On the influence of the geometrical irregularities in the mechanical response of Wire-and-Arc Additively Manufactured planar elements

Vittoria Laghi, Michele Palermo, Giada Gasparini, Valentina Alena Girelli, Tomaso Trombetti

On the influence of the geometrical irregularities in the mechanical response of Wire-and-Arc Additively Manufactured planar elements

In: Journal of Constructional Steel Research, Volume 178, 2021

On the influence of the geometrical irregularities in the mechanical response of Wire-and-Arc Additively Manufactured planar elements

Vittoria Laghi*, Michele Palermo Ph.D, Giada Gasparini Ph.D, Valentina Alena Girelli Ph.D, Tomaso Trombetti Ph.D

*corresponding author: vittoria.laghi2@unibo.it

Department of Civil, Chemical, Environmental and Materials Engineering - University of Bologna, Viale del Risorgimento, 2 – 40136 Bologna, Italy

Abstract

The use of Additive Manufacturing (AM) technologies in the construction industry is still at its pioneering stage. The first investigations indicate that, among actually available metal 3D-printing strategies, Wire-and-Arc Additive Manufacturing (WAAM) process appears to be the most suitable for realizing large-scale steel structures. Nonetheless, the limited knowledge of the mechanical response of WAAM alloys requires further experimental work for a reliable evaluation of the structural behavior of WAAM structural members. One specific issue which still needs to be fully investigated is the peculiar geometrical irregularity resulting from WAAM process that could have non-negligible effects on the mechanical behavior, such as anisotropy and non-homogeneous stress-strain fields. The present work explores the influence of inherent geometrical irregularities of WAAM stainless steel plates on the tensile response. For this purpose, detailed geometrical characterization of the external surface of WAAM specimens was carried out with 3D scanning techniques and random field theory. Different sets of specimens were subjected to tensile tests to evaluate the influence of surface finishing, orientation and cooling strategy. The whole strain field was studied through Digital Image Correlation (DIC) monitoring technique. Key findings are given in terms of geometrical characterization of surface roughness and thickness variability, as well as a quantitative assessment of the influence of geometrical irregularities on the main mechanical parameters. The material response reveals a significant anisotropy related to a marked crystallographic micro-texture. The geometrical irregularities negatively impact some of the mechanical parameters of the as-built material, suggesting further considerations for practical structural design applications.

Key words

Additive manufacturing; Experiment; Wire-and-arc; Stainless steel; Geometrical irregularities; Tensile testing; Digital Image Correlation.

1. Introduction

Among various Additive Manufacturing (AM) techniques, the most suitable for producing large metal components for construction industry is the so-called Wire-and-Arc Additive Manufacturing (WAAM). WAAM is classified as a Direct Energy Deposition (DED) process which combines an electric arc as heat source and a commercial welding wire as feedstock material [1]. The WAAM technique adopts higher deposition rates, allowing for a relatively fast production (2 to 10 kg/hour) of real-scale large structural components.

The main advantage of such innovative manufacturing technology lies in the freedom it offers when realizing any type of designed geometry. It allows for the realization of free forms and architecturally appealing shapes that are almost, in principle, without any geometrical constraints. Nonetheless, the high printing velocity required to produce large-scale elements results in visible geometrical discrepancies and imperfections, especially in terms of surface roughness (due to the layer-by-layer printing strategy), lack of straightness and non-uniform cross-sections [2–4].

Recent studies in the field of AM-based techniques applied to metal structures have focused on possible applications of 3D-printed technologies to the construction field and have provided initial data on the mechanical response of the printed material [4–7]. Other studies have been carried out to characterize the microstructural properties of WAAM alloys [8–15], with the main focus on the influence of process parameters and orientation of the specimens with respect to the printing layers on the microstructure. Up to date no specific studies were dedicated to the surface irregularities of WAAM elements.

A wide experimental campaign and extensive research work has been carried out at University of Bologna since 2017 with the main goal of providing guidelines for the structural design using WAAM-produced members. Investigations included mechanical, geometrical and microstructural analyses. The first mechanical and microstructural tests performed on machined specimens revealed an inherent material anisotropic behavior induced by the manufacturing process [16]. The first studies on the geometrical features indicated non-negligible geometrical discrepancy between the digital input used as reference model for the printing process and the real outcome [17,18]. Similar results were also presented in the work carried out by [6,7].

The present work provides an insight into the influence of the geometrical irregularities in terms of thickness variation and surface roughness inherent of the manufacturing process on the tensile stress-strain response of as-built WAAM-produced stainless steel elements.

2. Previous experimental campaign and research work

This section provides an overview of the main results of the experimental campaign on WAAM-produced stainless steel carried out in the last few years at University of Bologna including:

- Geometrical measurements (Section 2.2.)
- Mechanical tests (Section 2.3)
- Microstructural analysis (Section 2.4).

This research work allowed to characterize the basic properties of WAAM-produced stainless steel material from both geometrical, microstructural and mechanical points of view. The interested reader may find all the details in [16,17]. The aim of this section is to provide the reader with the information useful for a better understanding of the results and their interpretation presented in the paper (Sections 3 to 6).

2.1 Material and process

The precise specifications of WAAM process parameters are crucial to obtain elements characterized by the desired geometrical precision and expected structural response since such parameters can significantly affect both the geometrical and microstructural features of the printed outcomes.

The WAAM process here investigated is based on a printing set-up which consists of off-the-shelf welding equipment, such as welding power source, torches and wire feeding system, while motion is provided by either robotic system or computer numerical-controlled gantries.

The WAAM plates tested were realized by MX3D [19] with a commercially available standard stainless steel welding wire grade ER308LSi (1 mm diameter) supplied by *Oerlikon* [20]. All plates tested so far have been manufactured with the same set of process parameters whose values lie within the ranges shown in Table 1 (for more precise information the interested reader can refer directly to MX3D). The welding source used is Gas Metal Arc Welding (GMAW), with pulse welding arc transfer. No arc correction has been adopted during the printing process. The substrate is a printing plate of 1000 x 1000 x 30 mm, with H-type beams welded as support.

Process parameters	**Details**	**Value**
Deposition power	Current Arc voltage	100 - 140 A 18 - 21 V
Speed	Welding speed Wire feed rate	15 - 30 mm/s 4 - 8 m/min

	Deposit rate	0.5 - 2 kg/h
Distance and angle	Layer height Electrode to layer angle	0.5 - 2 mm 90°
Wire	Wire grade Wire diameter	ER308LSi 1 mm
Shield gas	Shield gas type Shield gas flow rate	98% Ar, 2%CO_2 10-20 L/min

Table 1: Process parameters for WAAM deposition (Courtesy of MX3D [19]*).*

It should be noted that the present study is based upon the printed outcomes resulting from the printing process having the parameters as presented in Table 1. For different sets of parameters, different surface finishing can be obtained.

WAAM's layer height is commonly in the range of 1 to 2 mm, resulting in an expected surface roughness up to 1 mm for single track deposit. As a result, this process is not considered net shaped, as machining is, in some cases, required to finish the part, thus being better suited for low- to medium-complexity and medium- to large-scale elements, as those implemented in structural engineering [1,4] (Figure 1). For instance, the first steel footbridge manufactured with this technology by MX3D will be placed with not-machined surface [21].

For ready-to-use elements and future applications of on-site metal 3D printing, it becomes crucial to study the geometrical irregularities and their possible influence on the mechanical response of WAAM-produced structural elements. Figure 1 displays the typical surface of a plate obtained with WAAM from which both as-built and machined specimens can be obtained.

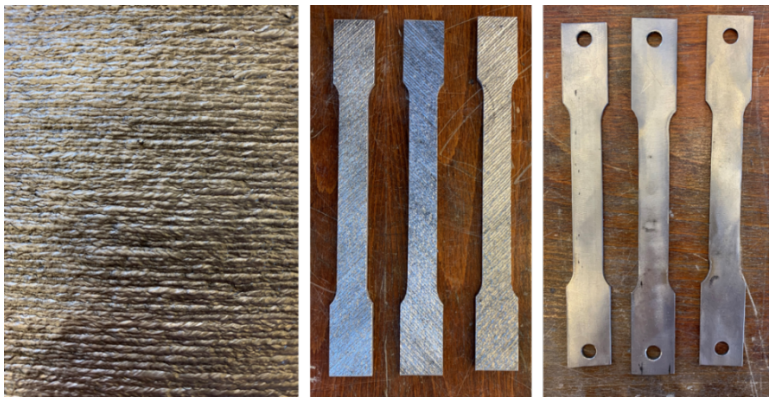

(a) (b) (c)

Figure 1: From left to right: (a) the inherent surface roughness of a WAAM printed plate; (b) as-built specimens; (c) machined specimens.

Therefore, from a structural design perspective it is of fundamental importance to characterize the main geometrical features of the printed surface and its influence on the mechanical response of WAAM-produced specimens.

2.2 Geometrical investigation

The first investigations on the geometrical properties of WAAM-produced stainless steel were carried out on different types of specimens, including dog-bone shaped specimens for tensile tests, stub columns coupons and tubular elements with circular cross-section. The investigations focused on the evaluation of the main geometrical imperfections related to the surface roughness of the dog-bone specimens, as well as the out-of-roundness and lack-of-straightness of tubular members. The results of the study have been presented in [17].

In detail, given the rough geometry of the printed outcomes, the first characterization focused on the geometrical discrepancies between the nominal digital input of the geometry (i.e. nominal thickness or nominal diameter, taken as input for the printing process) and the printed results. Two types of results were derived: (i) effective values of thickness (t_{eff}) and cross-sectional area (A_{eff}) used for the interpretation of the mechanical tests (see Sections 2.3 and 3.2) and (ii) some first information on the surface roughness and lack of straightness for engineering evaluations and future advanced modelling approaches.

From these first results it appeared that, in order to fully characterize WAAM-produced ready-to-use structural members, a more detailed study on the inherent geometrical irregularities is required.

2.3 Mechanical investigation

The first series of mechanical tests were performed on the same types of specimens on which the geometrical investigation has been carried out. In particular, the first two series of tensile tests were performed on machined and as-built dog-bone shaped specimens cut from rectangular plates, whereas compressive tests were performed on both stub columns and hollow circular tubes having different lengths. The results were presented in [17].

The results of the mechanical tests on as-built specimens (i.e. having the inherent geometrical irregularities proper of WAAM process) were interpreted assuming the equivalent constant cross-sectional area (referred to as effective area, A_{eff}) to compute the corresponding effective stress. The effective cross-sectional area is taken from average values as obtained from volumetric measurements (according to the Archimedes' principle), with the advantage of providing an integral value based on

equal weight criterion [17]. The same approach has also been recently adopted by Kyvelou et al. [7] to obtain the key mechanical properties of WAAM-produced as-built stainless steel specimens.

The first series of tensile tests were performed on machined specimens, to erase the geometrical discrepancies and thus focus only on the intrinsic material properties. The tests were carried out on three different specimens, oriented along three main directions with respect to the printing deposition layer (i.e. longitudinally, along the printing layers, transversally, perpendicular to them, and diagonally, at 45° inclination from them). The experimental results revealed a marked anisotropic behavior, especially for values of Young's modulus and elongation at rupture. In particular, Young's modulus values (105 GPa for transversal specimens and 130 GPa for longitudinal ones) were 40% to 60% lower than the standard value (200 GPa) for stainless steel, while those for diagonal specimens (230 GPa) resulted 20% higher than the standard. Reasonings of such anisotropic behavior are related to the microstructural crystalline orientation of the WAAM-produced stainless steel (see Section 2.4). Nevertheless, 0.2% proof stress and ultimate tensile strength values remained close to the traditionally manufactured stainless steel standards [16].

The results of the series of tensile tests conducted on as-built dog-bone specimens revealed, overall, the same trends (marked anisotropy) along the two perpendicular directions, with Young's modulus values in the range of 110-130 GPa for longitudinal and transversal specimens, and 0.2% proof stress and ultimate tensile strength in line with the values commonly adopted for traditionally manufactured stainless steel [17] as also encountered for the machined specimens, even though some slight differences were evidenced [16], probably to be attributed to the effect of the geometrical irregularities.

2.4. Microstructural analysis

Microstructural characterization of WAAM-produced stainless steel material was conducted at the Metallurgic laboratory of the University of Bologna to correlate the key mechanical properties with the microstructural features of the printed outcomes. In detail, microstructural analysis was carried out by means of 3D-Digital Microscopy (Hirox KH-7700), Reflected Light Optical Microscopy (RLOM) and Scanning Electron Microscopy (SEM) equipped with energy dispersive X-ray spectroscopy (EDS). The results were presented in [16].

In particular, the results revealed an anisotropic grain growth. Indeed, it clearly appeared that the WAAM process produced grains oriented perpendicular to the deposition layers, thus altering the mechanical response of specimens oriented at different directions with respect to the printing layers [16]. No significant defects (such as microcracks, inclusions or porosity) were detected on any of the

specimens tested, while density measures further confirmed the absence of porosity in the WAAM-produced material [16]. Specimens taken at different heights with respect to the base plate were characterized, and no significant influence of the thermomechanical history of the printed plates on the microstructure of the specimens was evidenced.

Figure 2 depicts the orientation of grain growth with respect to the deposition layer for specimens oriented along transversal direction. For the interested reader, further details can be found in [16].

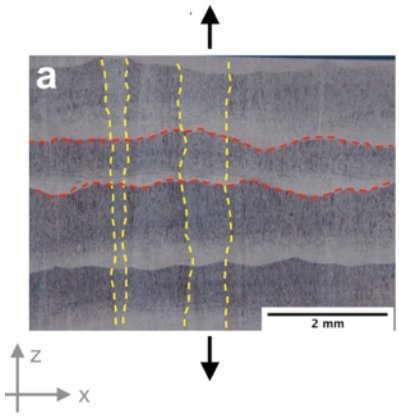

Figure 2: Microstructural grain growth (yellow) vs. deposition layer (red) for specimens oriented transversally. Black arrows indicate the loading direction (adapted from [16]*).*

3. Experimental tests on the influence of the geometrical irregularities on the mechanical response

From the previous research work (as presented in Section 2), it appeared that the anisotropic behavior evidenced from the results of the mechanical tests comes mainly from the orientation of the microstructural grains which affects the response under tensile loading. Moreover, the experimental results also evidenced some differences in the values of the key material properties of machined and as-built specimens, thus revealing a possible further influence of the geometrical irregularities on the mechanical response. Thus, the purpose of the present work is to fully characterize the inherent geometrical irregularities of as-built WAAM-produced specimens (Section 4) and investigate the possible influence of the geometrical imperfections in the mechanical response of as-built printed specimens (Section 5).

For such reason, a new experimental campaign has been carried out at the Structural Engineering and Metallurgic Labs of University of Bologna to characterize a series of planar specimens cut from plates realized with WAAM process and ER308LSi wire. A total number of ten plates with nominal planar dimensions of 380 mm x 380 mm and nominal thickness t_n= 4 mm were realized at MX3D facilities [19] and then tested at University of Bologna labs. The plates were realized with WAAM process by

depositing layer upon layer of welding material on a steel build plate (i.e. the plate lies on a plane perpendicular to the build plate).

From them, 44 specimens were tested with the purpose of evaluating the influence of the following main factors on the mechanical material behavior:

- surface finishing (as-built or machined);
- specimen orientation (parallel or perpendicular) with respect to the deposition layers;
- cooling strategy of printing.

As mentioned in Section 2, the inherent geometrical irregularities of WAAM-produced elements can possibly induce some non-negligible variations in the mechanical response of the specimens, in terms of concentration of stresses and non-uniform strain distribution, which should therefore be taken into account. As such, 32 specimens with as-built surface ("rough" R) and 12 with machined surface (M) were tested.

Considering the nature of the printing process, each plate was manufactured through successive printing deposition layers oriented along one main direction (x). Thus, the geometrical irregularities due to printing process, leading to a point-by-point variable thickness $t_{real}=t(x,y)$, result in a surface roughness with a peculiar texture and different features along two main directions based upon the printing direction. Indeed, one direction is along the printing layers (x) and the other one is perpendicular to them (y). Therefore, half of the machined (M) and as-built specimens (R) were taken along longitudinal direction (L), i.e. along the deposition layers, and the remaining parts along the transversal direction (T), i.e. perpendicular to them, as illustratively depicted in Figure 3.

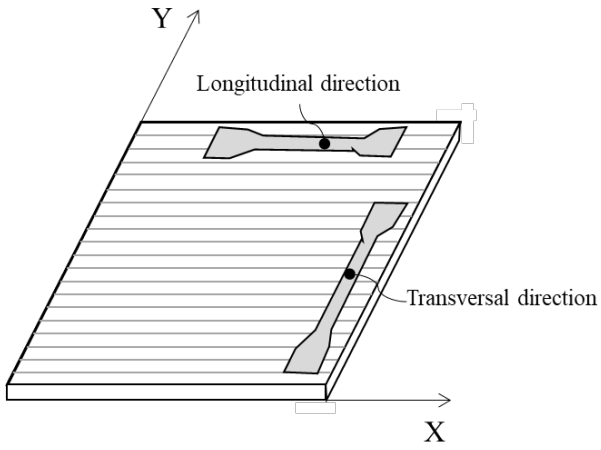

Figure 3: Orientation of WAAM-produced specimens: longitudinal (L) along printing deposition layers; transversal (T) perpendicular to them.

Two different cooling strategies were considered and their influence tested on the mechanical point of view. In particular, for each surface type and orientation half of the specimens were taken from the plates printed with active cooling system (A), consisting of blowing compressed air on the printed layer before depositing the successive one, thus reducing the waiting time between two deposition layers. The remaining ones were cut from the plates printed with uncontrolled cooling (U). Table 2 summarizes the types of specimens tested.

In order to provide quantitative measures of surface roughness and cross-section variation, a geometrical characterization of the specimens was first carried out (Section 4). First, a detailed evaluation of both surface roughness and distribution of thickness has been developed from 3D scanning measurements on one single as-built specimen. Then, a global evaluation of the effective thickness from volume measures has been carried out on all 44 specimens tested. The mechanical response of the specimens has been evaluated through tensile tests (Section 5). The response during the tests has been monitored through optical measuring system, referred to as Digital Image Correlation. The purpose was to evaluate the influence of surface roughness and non-uniform cross-sectional area in the tensile response of the specimens, both in terms of key material properties and with a specific focus on the strain field.

Surface type	**Orientation**	**Printing process**	**Quantity**	**Specimen ID**
Machined	Longitudinal	Active cooling	3	M-L-A-1 to M-L-A-3
		Uncontrolled cooling	3	M-L-U-1 to M-L-U-3
	Transversal	Active cooling	3	M-T-A-1 to M-T-A-3
		Uncontrolled cooling	3	M-T-U-1 to M-T-U-3
As-built (“rough”)	Longitudinal	Active cooling	8	R-L-A-1 to R-L-A-8
		Uncontrolled cooling	8	R-L-U-1 to R-L-U-8
	Transversal	Active cooling	8	R-T-A-1 to R-T-A-8

		Uncontrolled cooling	8	R-T-U-1 to R-T-U-8

Table 2: Specimens tested.

3.1. Geometrical characterization

In order to characterize the thickness and cross-sectional area of both as-built and machined dog-bone shaped specimens, different types of measures were performed.

A detailed investigation on the surface roughness and distribution of thickness proper of the WAAM process has been performed on one specific specimen (not tested in tension) using 3D scanning technique. The specimen was taken along the longitudinal direction (L), and printed with active cooling (A). The surface has been left as-built (R) to properly characterize its roughness. From the whole 3D model, the point-clouds of the two surfaces (upper and lower ones) have been processed in terms of their roughness, treating their heights (z coordinates) as two distinct random variables, whose main descriptors have been estimated according to ISO 25178-2 [22]. Then, from the whole 3D model a series of cross-sections along both directions (x and y, i.e. along the deposition layers and perpendicular to them) has been extracted and the thickness analyzed according to random process theory.

The instrument adopted for the 3D scan acquisition is a structured-light projection Artec Spider 3D scanner [23], an optical non-contact system for measuring the 3D surface of objects using a projector of blue light pattern and a camera. The projected light pattern on the object surface evidences distortions due to the specimen's surface shape, while the camera captures these distortions and permits the reconstruction of the surface 3D model by means of topographic triangulation principles. The instrument acquires full-field scans of a volumetric area and is able to collect millions of points per scan. More in detail, the specific instrument used in the present work is characterized by an acquisition speed of 1 mln points/sec for metrology applications. The obtained 3D resolution is 100 points/mm^2, with a 3D point accuracy of 0.05 mm for a medium field size of 90x70 mm and a working distance of 0.25 m.

The 3D model of the scanned planar specimen consists of around 40 millions triangular elements, with a medium points spacing of about 0.10 mm. Figure 4 shows a view of the entire mesh (blue model) and a zoom of it.

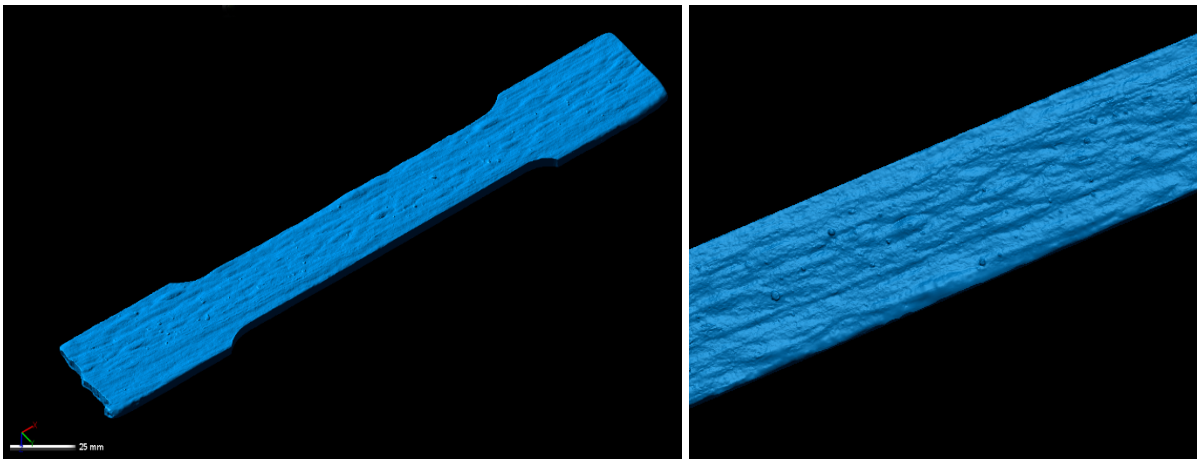

(a) (b)

Figure 4: (a) 3D model of one specimen cut along longitudinal (L) direction and (b) a zoom of it.

From a global perspective, the effective cross-sectional area A_{eff} of as-built specimens has been characterized by means of volume measurements, based on the Archimedes' principle [6,17], while the machined specimens have been characterized through multiple measurements with digital caliper (having a nominal precision of 0.01 mm) considering 20 cross-sections for each specimen.

3.2. Mechanical characterization

The mechanical characterization was carried out by performing uniaxial monotonic tensile tests on specimens shaped according to ISO 6892-1 [24].

As presented in Table 1, part of the specimens has been previously machined in order to erase the surface roughness and cross-section irregularities proper of the WAAM process [17,18]. Images of the specimens before and after surface milling are shown in Figure 5 (a-b). Clearly, the machining process determined a reduction of thickness for the machined (M) specimens with respect to the nominal 4-mm thickness of the plates. The stress-strain curves for the as-built (R) specimens were evaluated considering an effective homogeneous cross-sectional area taken from volume equivalency, as presented in Section 2.2 and previously adopted by [7,17].

Figure 5: Tensile specimen cut from WAAM plates: (a) as-built and (b) machined.

The tensile tests were performed according to ISO 6892-1 [24] on a Universal testing machine of 500 kN load capacity. The specimens were tested in displacement-control with a loading rate of 2 MPa/s. The strain values were obtained from optical system adopting Digital Image Correlation (DIC) technique to monitor the full strain field during the entire test. Additional Linear Variable Displacement Transducer (LVDT) with 50 mm gauge length was adopted for comparison of strain measures up to yielding. The tensile test set-up is presented in Figure 6.

Elastic Modulus (E), 0.2% proof stress ($Rp_{0.2}$), ultimate tensile strength (UTS) and elongation at rupture ($A_{\%}$) were evaluated from the engineering stress-strain curves. The density of WAAM samples was determined by means of volume-based measures taken with a hydraulic scale according to the Archimedes' principle.

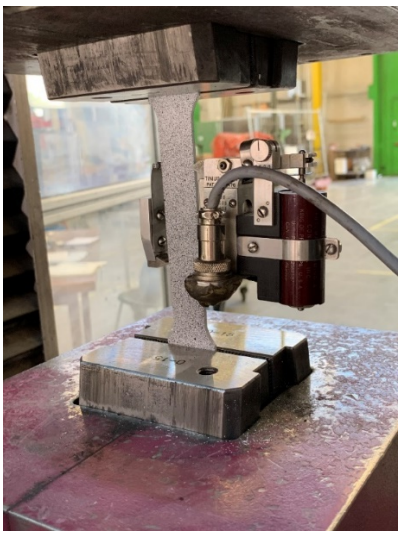

Figure 6: Tensile test set-up.

4. Results from geometrical characterization

4.1. Surface roughness

The 3D model obtained from 3D scanning was first analyzed in terms of surface roughness, considering separately the two point-clouds of the upper and lower surfaces. For each surface the origin of the reference axis (z-axis) has been placed in order to obtain an ensemble of z_i points having zero-mean (i.e. the mean value of the z_i coordinates is zero for both surfaces). The set of z coordinates of each surface can thus be considered as an individual random variable, namely Z_{US} (for the upper surface) and Z_{LS} for the lower surface. In general, the two random variables could be correlated therefore they are not treated as independent random variables.

Data analysis has been carried out with an open-source GIS environment to gather information about the surface roughness in terms of peaks and pits (Figure 7). For this aim, the heights z of the points of each of the two surfaces (upper, z_{US}, and lower, z_{LS}) have been measured with respect to a horizontal plane x,y located at either the upper or the lower mean height. In this way, peaks and pits are identified as local maxima or minima of the function z directly by the software.

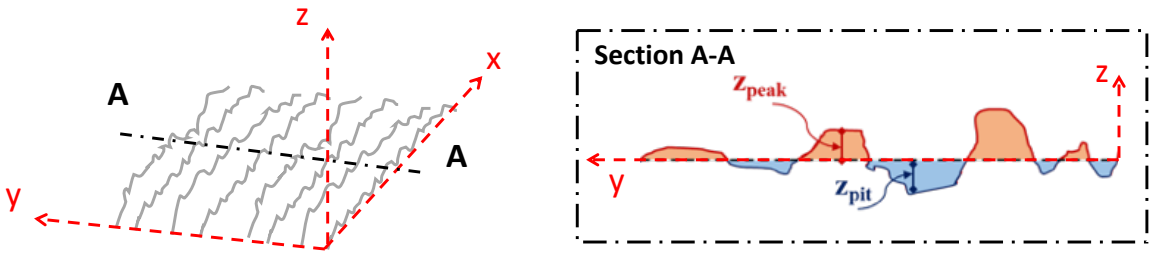

(a) (b)

Figure 7: (a) Qualitative graphical representation of the surface roughness; (b) section A-A from surface profile and evaluation of peaks and pits from z coordinates.

Figure 8 shows the locations of peaks (small red dots) and pits (small blue dots) on both the upper and lower surface. The ten largest values of peaks and pits are indicated with big dots. The location of peaks and pits allows to appreciate the path following the deposition layers, as the crests of the printing layers correspond to the peak lines while among each two successive printing layers lie the pit lines. These lines clearly mark the orientation of the specimen scanned, which is taken longitudinally (L), i.e. having the longitudinal axis along the direction of the printing deposition layers.

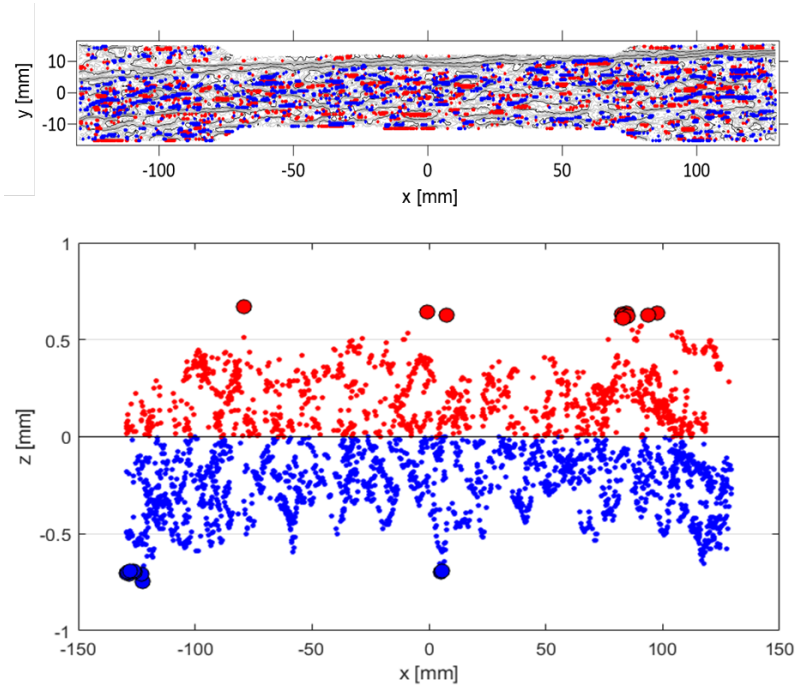

(a)

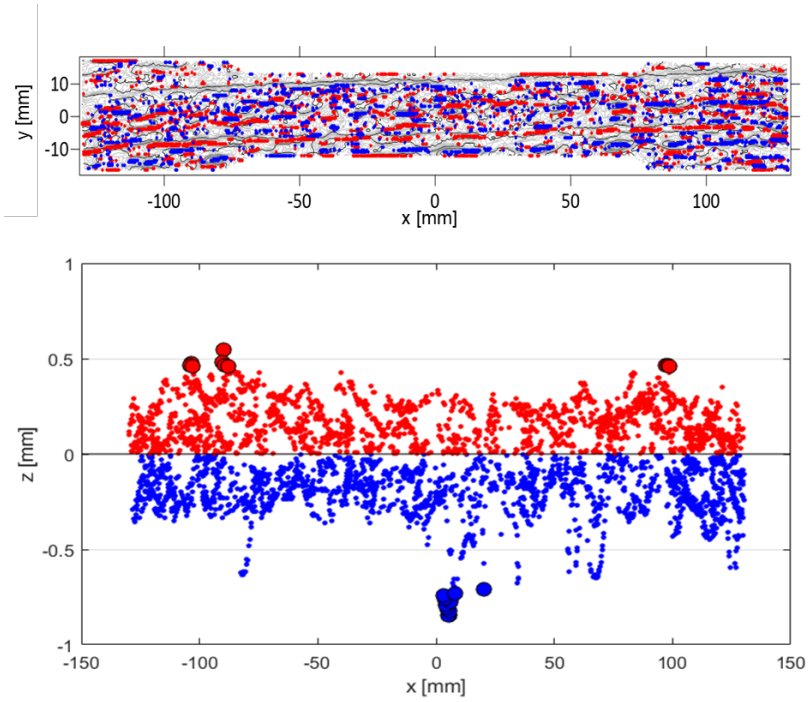

(b)

Figure 8: Distribution of peaks (red) and pits (blue) along the (a) upper and (b) lower surface of the 3D-scanned specimen.

The main features of the surface roughness can be quantitatively described in terms of the main descriptors identified by the standard ISO 25178-2 [22]: maximum peak height (S_p), maximum pit

height (S_v), arithmetical mean height (S_a), root mean square height (S_q), skewness (S_{sk}) and kurtosis (S_{ku}). The values of the main descriptors are collected in Table 3. The values labelled *US* refer to the upper surface, whereas those labelled *LS* refer to the lower surface.

Roughness parameters	**Formulation (according to [22])**	**Value (mm)**	
Maximum peak height (S_p)	$S_p = \max_A [z(x,y)]$	US	0.67
		LS	0.54
Maximum pit height (S_v)	$S_v = \min_A \lvert z(x,y) \rvert$	US	0.74
		LS	0.85
Arithmetical mean height (S_a)	$S_a = \frac{1}{A}\iint_A \lvert z(x,y) \rvert dxdy$	US	0.19
		LS	0.14
Root mean square height (S_q)	$S_q = \sqrt{\frac{1}{A}\iint_A z^2(x,y)dxdy}$	US	0.27
		LS	0.20
Skewness	$S_{sk} = \frac{1}{S_q^{\,3}}\left[\frac{1}{A}\iint_A z^3(x,y)dxdy\right]$	US	0.03
		LS	-0.14
Kurtosis	$S_{ku} = \frac{1}{S_q^{\,4}}\left[\frac{1}{A}\iint_A z^4(x,y)dxdy\right]$	US	2.73
		LS	3.38

Table 3: Surface roughness parameters evaluated according to ISO 25178-2 [22].

Maximum peaks and pits heights are in the range of 0.54-0.85 mm with no significant differences between the two faces. The values of the arithmetic mean heights and root mean square heights are between 0.14 and 0.27 mm. Although due to the groove-like surface the relative distributions of peaks and pits would be expected to be asymmetric, the results show that the skewness is close to zero for both upper and lower surfaces. This suggests the need for further investigations on the specific nature of the resulting roughness. The values of kurtosis are slightly larger or smaller than 3, suggesting a flatness similar to that of a Normal Gaussian distribution.

4.2. Thickness from 3D scanning acquisition

From the full 3D model generated by 3D scanning acquisition (consisting of 40 millions of points), an in-depth characterization of the thickness was carried out as well. The average (effective) thickness

of the specimen as taken from volume measurements (according to the Archimedes' principles, as also used in [7,17]) is 3.42 mm.

Given the marked orientation of WAAM planar elements due to the successive layers of deposited material, first a statistical analysis of the thickness distribution along the two directions x and y has been carried out. For this purpose, selected values of thickness $t(x_i,y_i)$ have been extracted from the 3D model discretizing a portion of specimen of 69 mm length as a grid (see Figure 9) with 3 mm spacing along the longitudinal direction (x) and 1.4 mm along the transversal direction (y) leading to N_x=23 measurements along x for a fixed value of y and N_y=14 measurements along y for a fixed value of x. The total number of measurements is therefore N_{tot}=322. Clearly, the thickness measurements indirectly provide also information on the correlation between the surface roughness of the upper and lower surfaces, even though based on a smaller dataset (see Section 6.1.1).

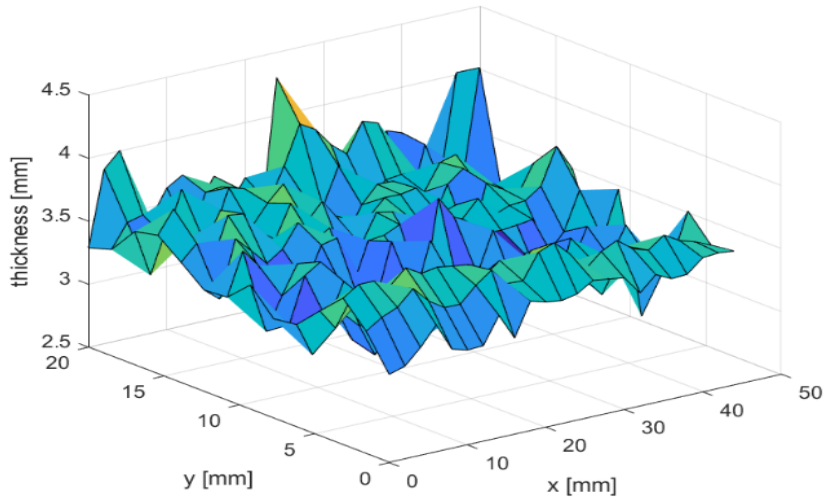

(a)

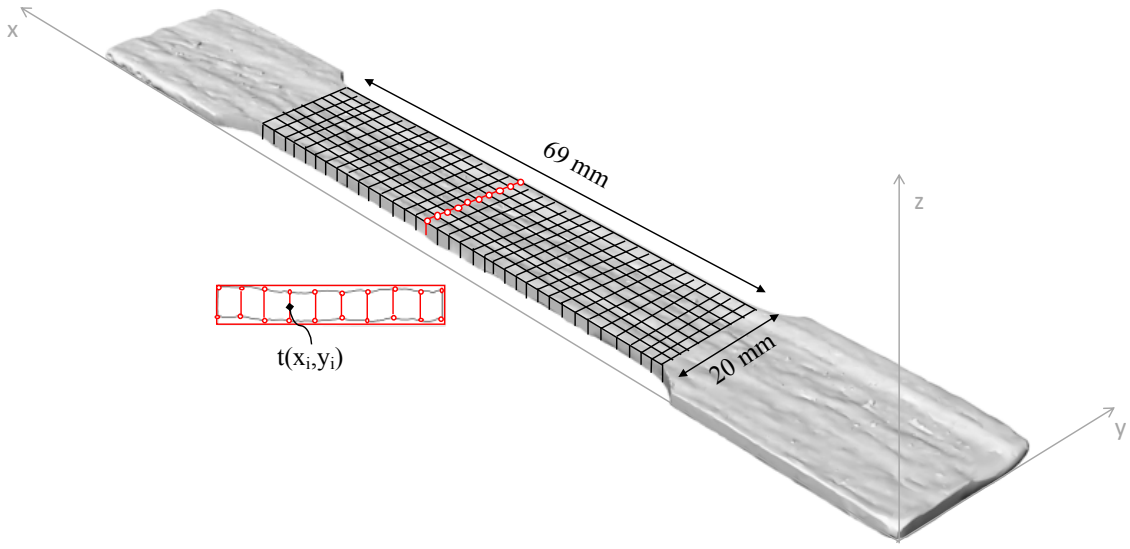

(b)

Figure 9: (a) 2D plot thickness distribution; (b) extraction of the thickness values $t(x_i,y_i)$ *from 3D model.*

For a fixed value of y_i, the set of measurements along the length (i.e. along the longitudinal direction x) $t(x|y_i)$ can be interpreted as the single realization of a random process $t(x)$. The set of all realizations $t(x|y_i)$ is typically called ensemble (Figure 10).

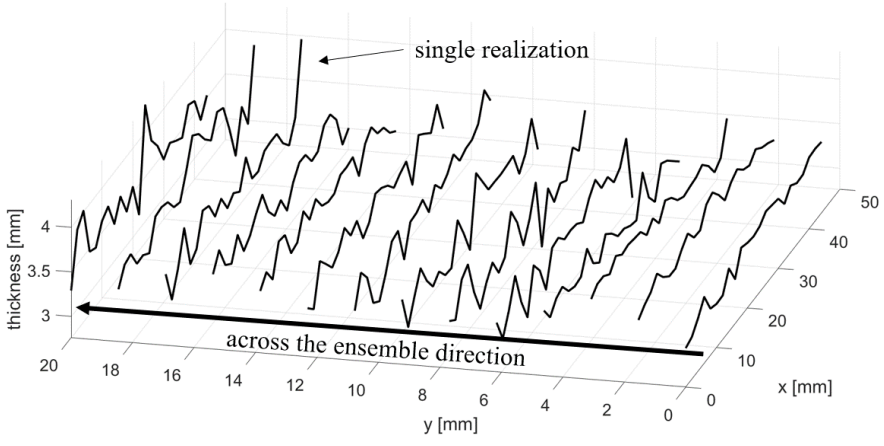

Figure 10: Plot of thickness measurements for fixed y values $t(x|y_i)$.

The main properties of the random process can be analyzed computing the statistics both across the ensemble (for a specific value x_i) and along the length (i.e. considering a single realization for a specific y_i) as reported in Table 4.

Statistical parameters	**Definition**	**Range**	**Mean +/- st.d**
Across-the-ensemble mean	$\mu_{t(x)} = \frac{1}{N_y}\sum_{i=1}^{N_y} t\left(x_j \mid y_i\right)$	[3.35 - 3.58]	3.48 ± 0.05
Across-the-ensemble standard deviation	$\sigma_{t(x)} = \sqrt{\frac{\sum_{i=1}^{N_y}\left(t\left(x_j \mid y_i\right) - \mu_{t(x)}\right)^2}{N_y - 1}}$	[0.11 - 0.38]	0.20 ± 0.06
Along-the-length mean	$\mu_{t(y)} = \frac{1}{N_x}\sum_{j=1}^{N_x} t\left(x_j \mid y_i\right)$	[3.26 – 3.63]	3.48 ± 0.12
Along-the-length standard deviation	$\sigma_{t(y)} = \sqrt{\frac{\sum_{j=1}^{N_x}\left(t\left(x_j \mid y_i\right) - \mu_{t(y)}\right)^2}{N_x - 1}}$	[0.09 – 0.25]	0.18 ± 0.05
Overall mean	$\mu_t = \frac{1}{N_y}\mu_{t(y)} = \frac{1}{N_x}\mu_{t(x)}$	3.48	
Overall standard deviation	$\sigma_t = \sqrt{\frac{\sum_{i=1}^{N_{tot}}\left(t(x_i, y_i) - \mu_t\right)^2}{N_{tot} - 1}}$	0.21	

Table 4: Statistical properties of thickness modelled as a random process.

Across-the-ensemble means and standard deviations are functions of x ($\mu_{t(x)}$, $\sigma_{t(x)}$), while along-the-length mean and standard deviations are functions of y ($\mu_{t(y)}$, $\sigma_{t(y)}$). Their trends, together with the related coefficients of variation, are represented in Figure 11.

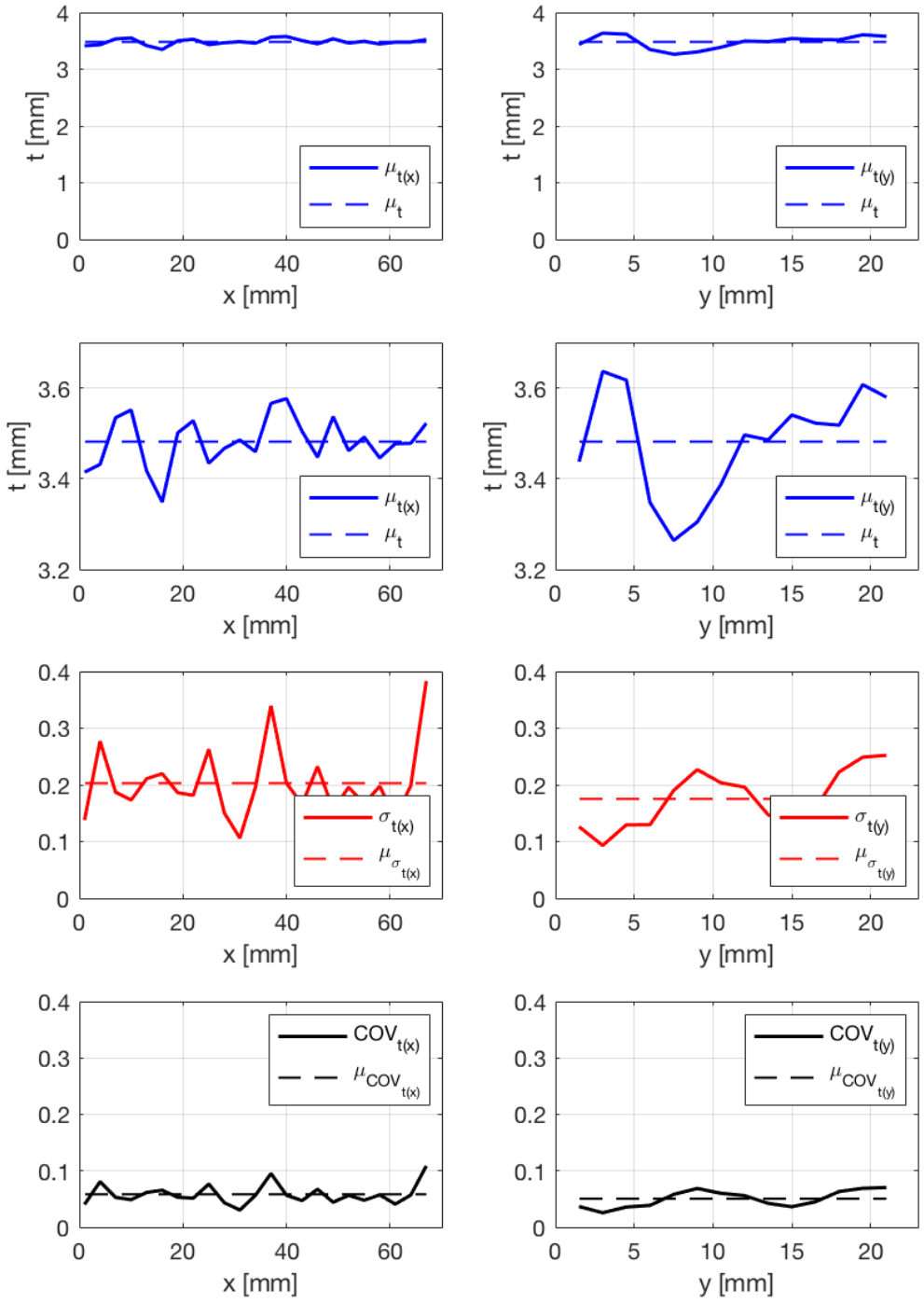

Figure 11: Across-the-ensemble (left-hand side) and along-the-length (right-hand side) mean and standard deviation trends.

The across-the-ensemble mean values $\mu_{t(x)}$ oscillate around 3.35 mm and 3.58 mm with small variability. This condition ($\mu_{t(x)} \cong \mu_t$) indicates that the process can be considered stationary in average sense, since the thickness does not significantly vary moving along the longitudinal direction (e.g. the printing direction). Indeed, the succession of peaks and pits across the ensemble is quite regular moving along direction *x*. The across-the-ensemble standard deviation values $\sigma_{t(x)}$ exhibit a relatively large variability (values between 0.10 mm to almost 0.40 mm) with an average value equal to 0.20 mm. This large variability is partially due to the variation of the mean value among different realizations (i.e. succession of peaks and pits).

The along-the-length mean values $\mu_{t(y)}$ have a larger variability (from 3.26 to 3.64 mm.) than the across-the-ensemble mean $\mu_{t(x)}$, thus indicating that the process cannot be considered ergodic in an average sense. Indeed, each realization (i.e. corresponding to specific values of y_i) may be taken either in the proximity of the deposition layers (i.e. peak values) or between two consecutive layers (i.e. pit values). The along-the-length standard deviation values $\sigma_{t(y)}$ do not significantly vary for different realizations and have an average value of 0.18 mm. Such value can be considered a measure of the intrinsic variability of the thickness, within a specific layer, thus related to the precision of the deposition process. Coefficients of variation are, on average, around 0.05-0.06, with maximum values around 0.1. Further interpretation is provided in the discussion of Section 6.1.

A correlation analysis was also carried out computing the correlation coefficient between all realizations $\rho(t(x|y_i))$ and between all sections taken across the ensemble $\rho(t(x_j|y))$. The corresponding correlation matrices are reported in Appendix (Tables A1 and A2). Overall, the correlation matrices confirm that there is no significant trend either along the length or across the ensemble.

For illustrative purposes, Figure 12 shows selected statistical distributions of thickness across the ensemble and along the length for a pair of consecutive or either far-located *y* or *x* points, together with their scatter graphs. In general, the distributions along *x* are quite random and tend to follow Gaussian-type distributions. The distributions along *y* tend to be more uniform with few peaks, possibly related to the consecutive distribution of peaks and pits.

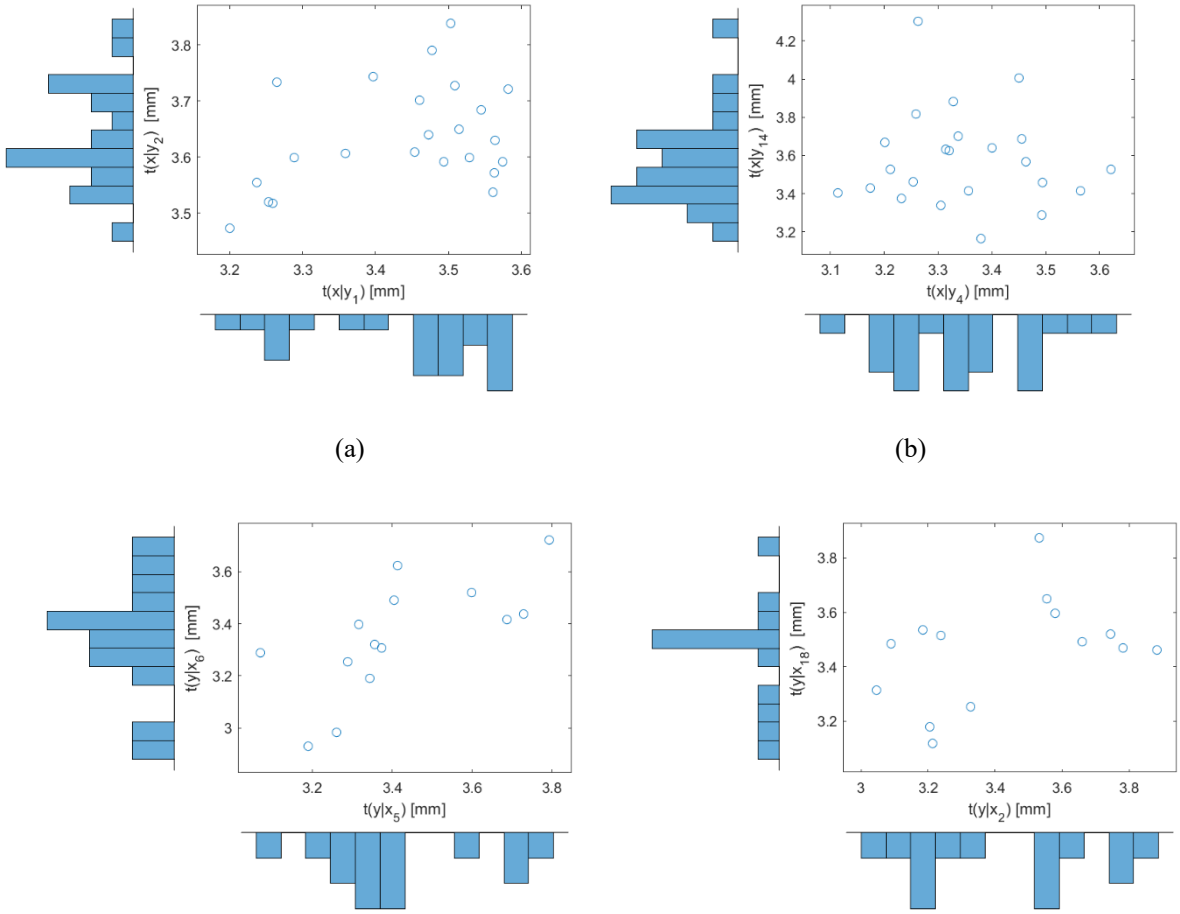

(a) (b)

(c) (d)

Figure 12: Distribution of thickness – (a) and (b) along x direction; (c) and (d) along y direction.

The overall statistical distribution considering all measured thickness values $t(x_i,y_i)$ is reported in Figure 13, in terms of both empirical cumulative distribution and relative frequency histograms. The estimations of the mean and standard deviation from the data are equal to μ_t= 3.48 mm and σ_t =0.21 mm, respectively, resulting in a coefficient of variation equal to 0.06. The skewness coefficient γ_t is equal to 0.07, thus indicating an almost symmetrical distribution. In the same graph also the best fit Normal and Lognormal statistical distributions are plotted. Their main parameters (mean value, standard deviation and skewness coefficient) are provided in Table 5. It can be noted that the best-fit Lognormal is practically coincident with a Normal distribution. This is clearly due to the small coefficient of variation and the very small skewness (the skewness value for the best-fit Lognormal is equal to 0.18). Table 5 also provides the KS values of the Kolmogorov-Smirnov test associated to the two best-fit distributions. The critical value for a significance level α=0.05 is equal to 0.07. Since both KS values are smaller than the critical one, both distributions can be considered a good fit of the

experimental distribution. Since the data are all positive and have a small asymmetry, the Lognormal distribution could be preferred.

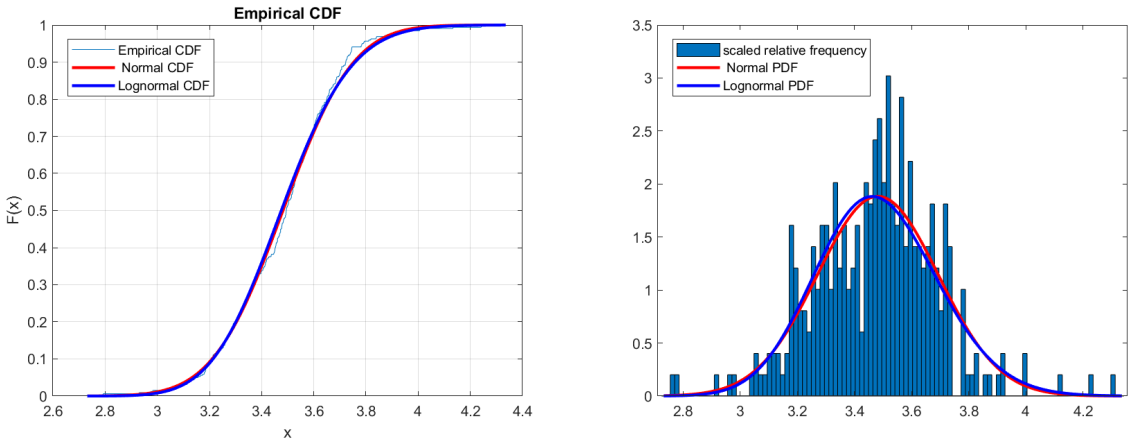

(a) (b)

Figure 13: Distribution of thickness for the 3D-scanned specimen: (a) CDF; (b) PDF.

Specimen Type	Surface Type	Measurement type	Distribution type	μ_t [mm]	σ_t [mm]	γ_t [-]	KS [-]
L	R (as-built)	3D scanning	Normal	3.48	0.21	0	0.055
			Lognormal	3.48	0.21	0.18	0.066

Table 5: Statistical parameters of the best-fit distribution of thickness along the 3D-scanned specimen.

4.3. Effective thickness from manual measurements

As explained in Section 3.1, the average thickness and cross-sectional area of the machined specimens (M) were measured with digital caliper. On the contrary, the effective thickness and cross-sectional area of the as-built specimens (R) were obtained from volume measurements. Table 6 presents an overview of the mean thickness values for both types of specimens. Clearly, the machined specimens resulted in a reduced mean thickness (average values equal to 2.85 for L specimens and 2.58 for T specimens) with respect to the as-built ones.

Specimen type	Surface type	Measurement type	$\mu_{t_{eff}}$ [mm]

L	M (machined)	Manual	2.85
T			2.58
L	R (as-built)	Volume	3.58
T			3.76

Table 6: Average values of thickness for the specimens tested.

The average effective thickness ($\mu_{t_{eff}}$) of the as-built specimens is equal to 3.58 mm for specimens oriented along the longitudinal direction (L) and 3.76 mm for specimens oriented along the transversal direction (T), thus resulting slightly lower that the nominal thickness t_n=4 mm. This result provides a first indication on the systematic difference between the effective as-built thickness and the nominal one, used as input from the printing process. Indeed, from volume-based measurements the difference $\Delta_{t,eff}$ is of 0.42 mm for L specimens and 0.24 mm for T specimens. The corresponding relative error between effective and nominal thickness (evaluated as (*effective- nominal)* / *nominal*) is of the order of -10% for L specimens and -6% for T specimens. The values of the standard deviations ($\sigma_{t_{eff}}$) are practically equal along the two directions (0.13 mm for specimens along L and 0.14 mm for specimens along T) and correspond to a coefficient of variation of around 0.04.

The discrepancy between the nominal thickness set as digital input in the printing process (4 mm) and the average effective one of the printed outcome (3.58 mm for L specimens, 3.76 mm for T specimens) is highly affected by the set of process parameters adopted (presented in Table 1). Different sets of parameters would result in general in a different surface finishing.

5. Results from mechanical characterization

5.1. Stress-strain response

Figures 14 and 15 show the whole engineering stress-strain curves and a zoom of them corresponding to a strain limit of 1%, respectively. Each graph compares the stress-strain curves of as-built (R, continuous lines) and machined (M, dashed lines) specimens for the same orientation and cooling strategy. In general, not so large discrepancy appears when comparing the responses of as-built and machined specimens with same orientation and cooling strategy (especially for active cooling, see details in Section 6.2).

Overall, when comparing the two different orientations, it can be noticed that the curves of specimens oriented transversally (T) are smoother with a less sudden transition between the elastic and plastic phase. This is particularly evident from the zoom showed in Figures 15. Moreover, specimens oriented along transversal direction evidence, on average, smaller values of ultimate tensile strength and elongation at rupture. The major difference when comparing specimens realized with active cooling (A) and with uncontrolled cooling (U) is also noticed in the values of elongation at rupture. Indeed, specimens with active cooling have elongation at rupture of around 20%, while those realized with uncontrolled cooling reach values up to 30-40%. A more in-depth discussion is provided in Section 6.2

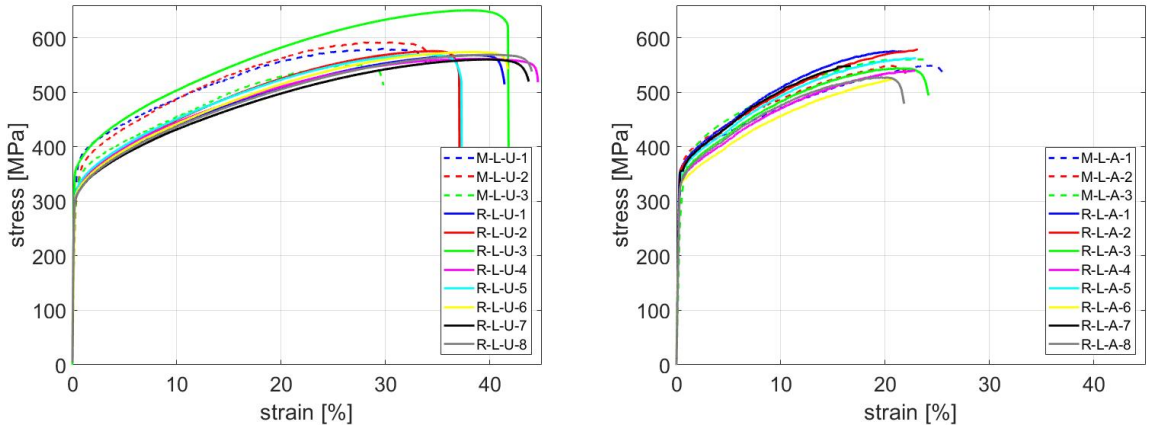

(a)

(b)

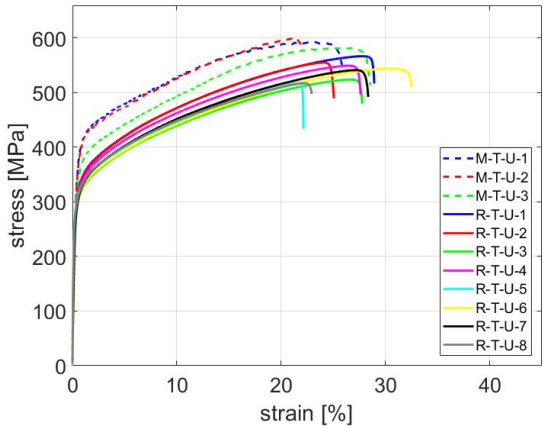

(c)

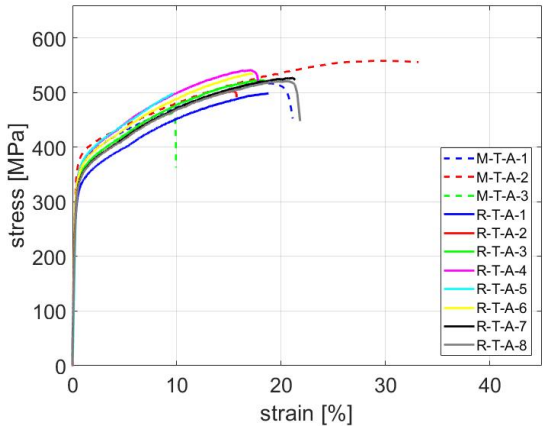

(d)

Figure 14: Stress-strain curves of tensile tests: (a) longitudinal (L) specimens with uncontrolled cooling (U) and (b) with active cooling (A); (c) transversal (T) specimens with uncontrolled cooling (U) and (d) with active cooling (A).

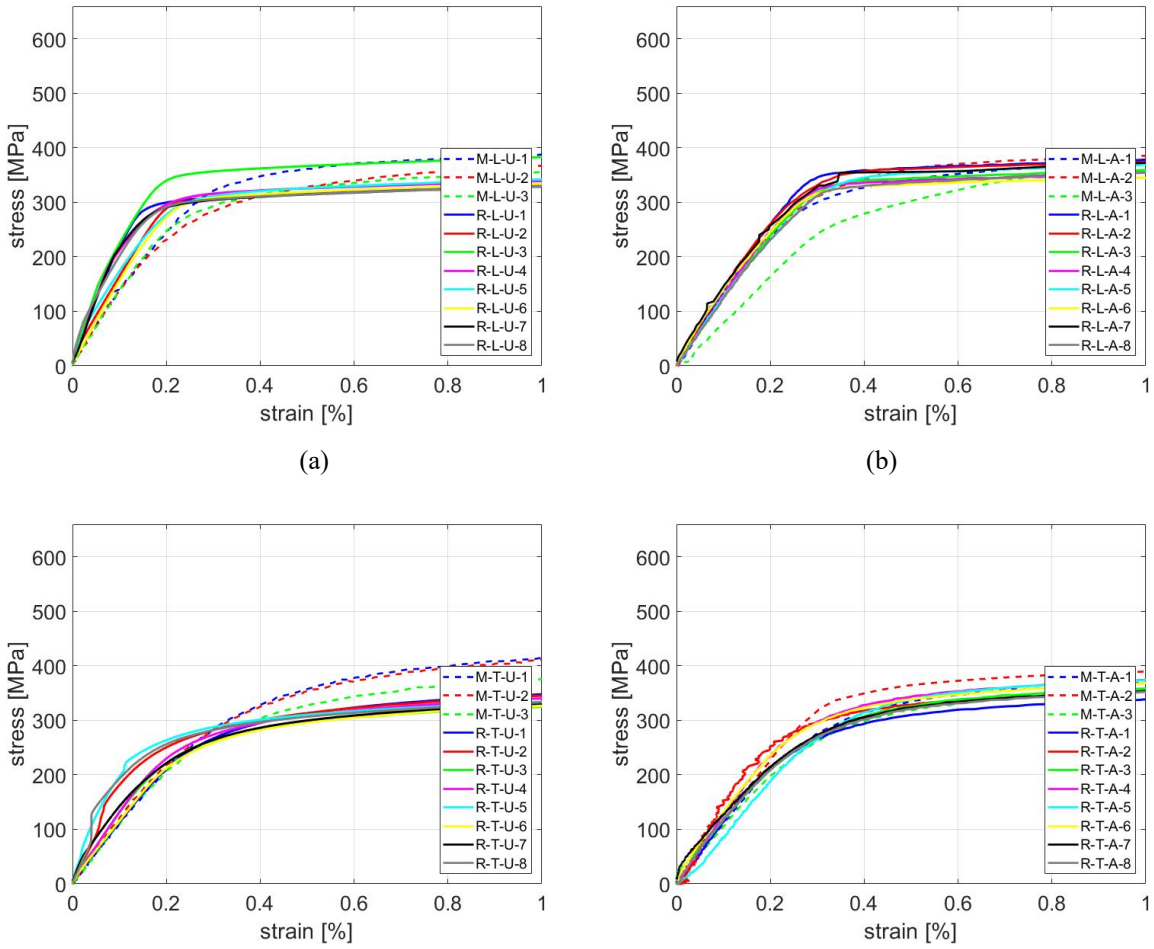

Figure 15: Stress-strain curves of tensile tests – zoom at deformations <1%: (a) longitudinal (L) specimens with uncontrolled cooling (U) and (b) with active cooling (A); (c) transversal (T) specimens with uncontrolled cooling (U) and (d) with active cooling (A).

Table 7 reports the mean values plus/minus one standard deviation of the key material parameters, i.e. Young's modulus (E), 0.2% proof stress ($R_{p0.2}$), ultimate tensile strength (UTS), elongation at rupture ($A_{\%}$) and yield to tensile strength ratio ($R_{p0.2}/UTS$) as obtained from tensile tests according to EN ISO 6892-1 [25] standards. Given that the most widely adopted material model for stainless steel is the two-stage Ramberg-Osgood formulation ([26–28]), also the strain hardening exponents n and m have been computed and reported in Table 7. In order to accurately evaluate the Young's modulus values overcoming the experimental noise typical of the stress-strain curves, the ordinary least squares regression (OLSR) analysis was employed, as proposed by ([7]).

Overall, quite low values of Young's modulus (on average, from 110 GPa to 130 GPa for machined (M) specimens, and from 110 GPa to 170 GPa for as-built (R) ones) are observed when compared to typical values of traditionally-manufactured stainless steel for structural members, according to

Eurocode 3 [29] (200 GPa). The work done by [7] reported even higher discrepancy between machined and as-built specimens, with however lower difference between values for specimens oriented transversally (T) and longitudinally (L), especially for machined specimens. Reasonings to these differences might be due to the different thickness of the specimens tested (of 8 mm for [7] vs. 4 mm as for the present study). Moreover, the results presented in this study reveal a non-negligible influence of the cooling strategy, which however was not clearly investigated in [7].

On the other hand, the values of 0.2% proof stress and ultimate tensile strength are in line with respect to those recommended by Eurocode 3 for traditionally-manufactured stainless steel [29]. Those findings are in line with the results of the previous experimental tests carried out by the authors in [16,17] and found in literature [6], as already highlighted in Section 2.3.

Concerning the strain hardening exponents, *n* values are quite scattered (from 7 to 15), while both *m* values and yield to tensile strength ratio ($R_{p0.2}$/ *UTS*) do not seem to be affected by the different orientations and printing strategy of the specimens tested. Similar results were also found in [7].

Surface type	**Specimen type**	**Printing strategy**	**Specimen ID**	**E [GPa]**	**$R_{p0.2}$ [MPa]**	**UTS [MPa]**	**$A_{\%}$ [%]**	**n [-]**	**m [-]**	**$R_{p0.2}$/ UTS [-]**
M	L	A	M-L-A	**133.02** ± 2.52	**355.73** ± 11.49	**552.60** ± 4.97	**22.71** ± 2.10	**8.29** ± 1.55	**3.14** ± 0.12	**0.64** ± 0.02
R			R-L-A	**132.51** ± 6.73	**345.78** ± 9.13	**546.71** ± 25.63	**21.79** ± 2.15	**10.47** ± 3.41	**3.22** ± 0.06	**0.63** ± 0.02
M		U	M-L-U	**142.22** ± 3.87	**335.08** ± 15.45	**574.73** ± 17.11	**32.80** ± 2.11	**14.75** ± 5.39	**3.04** ± 0.09	**0.58** ± 0.03
R			R-L-U	**173.76** ± 38.90	**317.57** ± 19.18	**578.73** ± 27.67	**41.48** ± 2.69	**14.23** ± 5.09	**2.91** ± 0.02	**0.55** ± 0.01
M	T	A	M-T-A	**111.59** ± 7.05	**351.47** ± 18.79	**513.14** ± 38.83	**21.41** ± 9.49	**12.88** ± 7.38	**3.33** ± 0.09	**0.69** ± 0.03
R			R-T-A	**116.72** ± 12.87	**325.04** ± 13.22	**518.33** ± 15.56	**17.77** ± 3.57	**7.77** ± 3.04	**3.16** ± 0.06	**0.63** ± 0.03
M		U	M-T-U	**111.30** ± 1.18	**353.60** ± 17.85	**591.92** ± 7.40	**25.54** ± 2.64	**7.14** ± 0.79	**3.09** ± 0.09	**0.60** ± 0.03
R			R-T-U	**125.32** ± 24.18	**295.68** ± 6.46	**539.56** ± 16.98	**27.00** ± 3.05	**10.55** ± 1.74	**2.90** ± 0.05	**0.55** ± 0.02

Table 7: Overview of the tensile test results.

5.2. Focus on the strain fields

The strain fields were analyzed through DIC monitoring system. The main purpose of the investigation is to evaluate the influence of the geometrical irregularities on the strain fields by analyzing the different strain distribution of as-built and machined specimens. Therefore, for the sake of conciseness, the results related to four specific specimens are discussed in detail: two machined (M) and two as-built (R) specimens oriented along the two orientations (M-L-A-2, M-T-A-1, R-L-A-8 and R-T-A-8). The four specimens considered were realized with active cooling strategy. However, a similar response was obtained for the specimens realized with uncontrolled cooling. For each specimen considered, the whole strain field was analyzed by comparing the local peak strain (ε_p) with the average strain (ε_m) evaluated along the gauge length ($\varepsilon_m = \frac{\Delta L}{L} \cdot 100$), see Figure 16. The results of this analysis are reported in Figure 17 for 10 relevant stages encompassing the whole range of behavior from the elastic field up to failure. The figure also represents colored maps of strain fields at selected stages with indication of the location of the peak strain. For all specimens, the location of the peak strain remained stable after reaching the first yielding up to failure. Table 8 reports the values of ε_p and ε_m and their relative discrepancies. On average, local peak strains are 50-60% larger than average strains. No appreciable differences are noticed when comparing as-built and machined responses. Thus, overall the geometrical irregularities do not seem to significantly alter the strain distribution during tensile tests. It should be noted that the position of rupture for all specimens lie within the gauge length, and does not suggest particular evidence of defects or rougher parts affecting the failure of specimens.

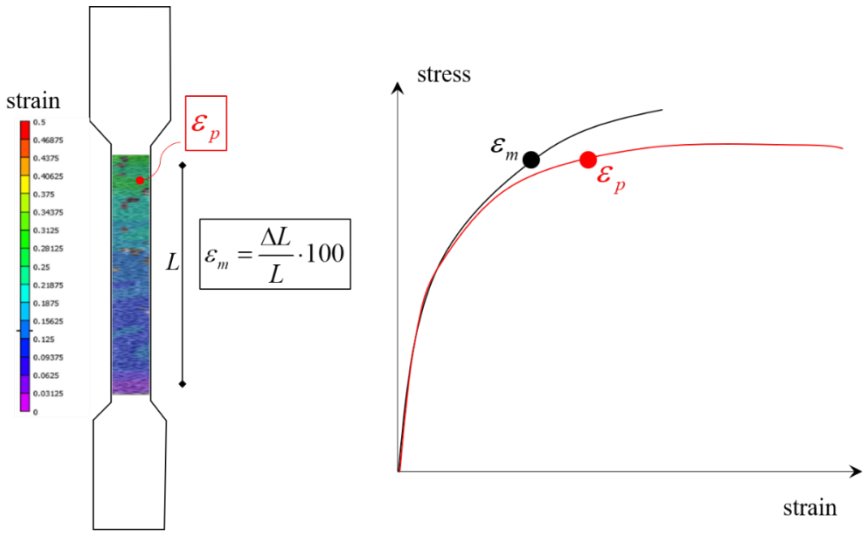

Figure 16: Qualitative representation of stress-strain curves from peak and average strains.

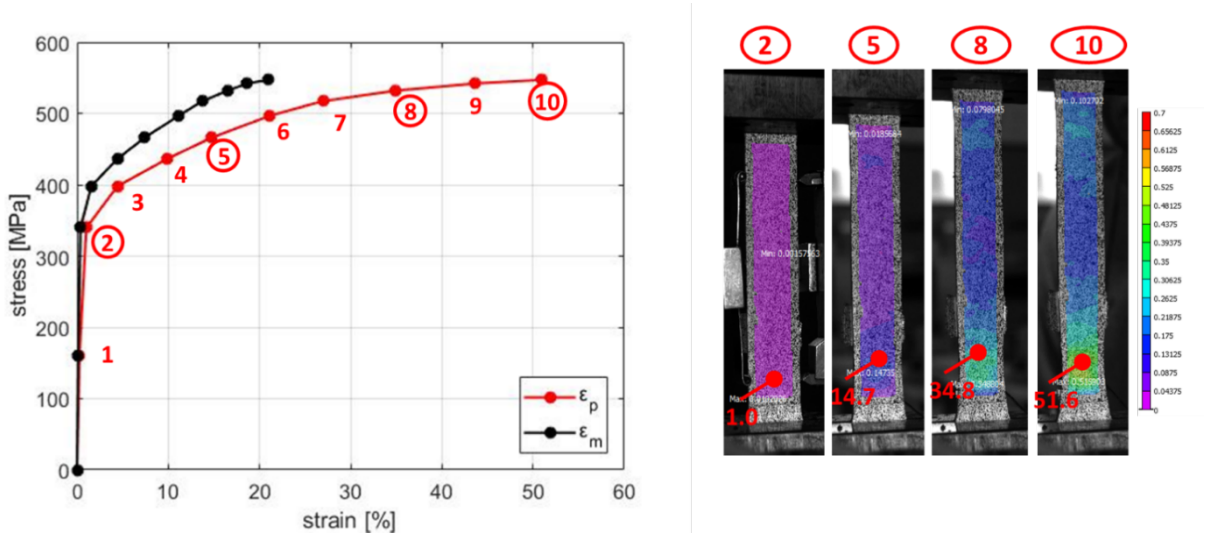

(a)

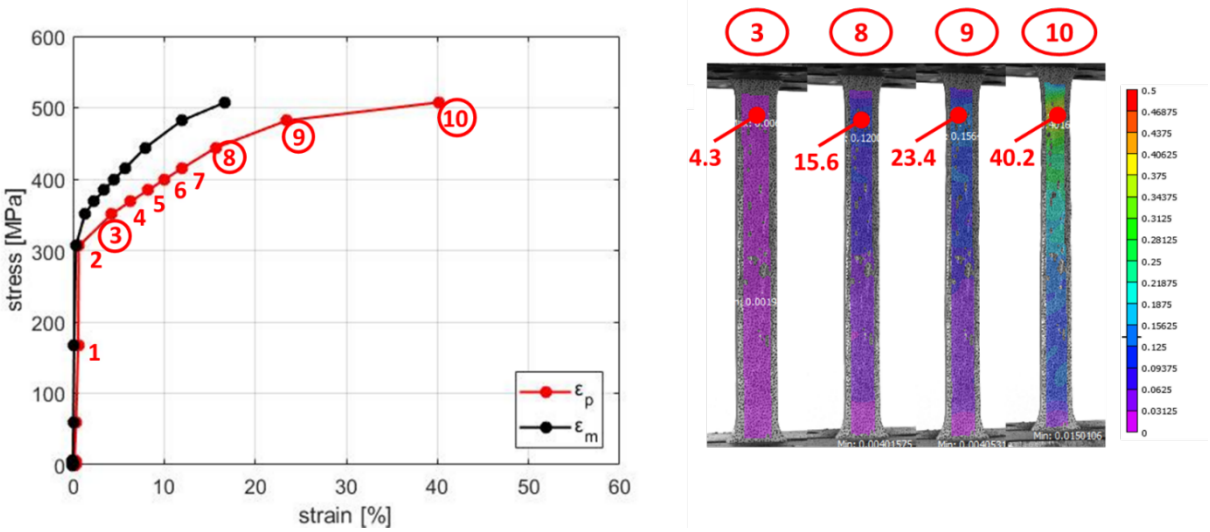

(b)

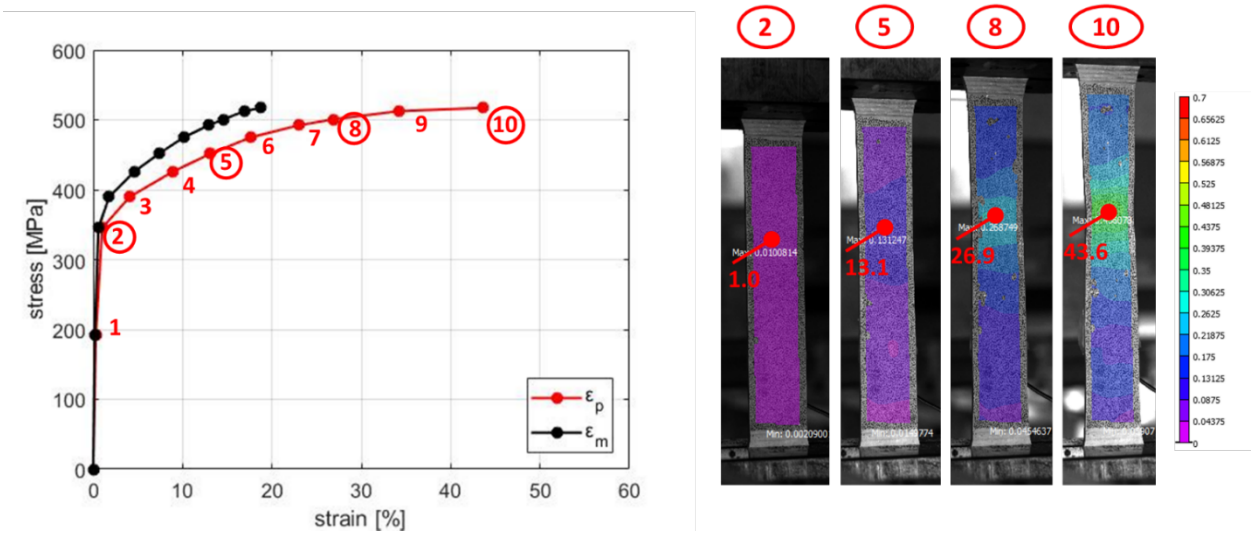

(c)

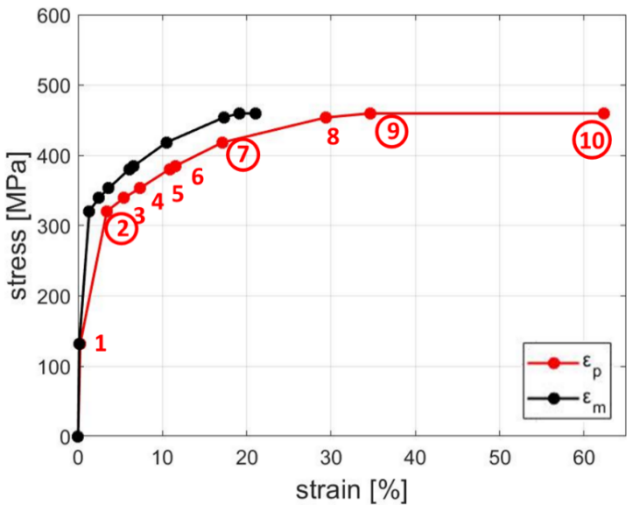

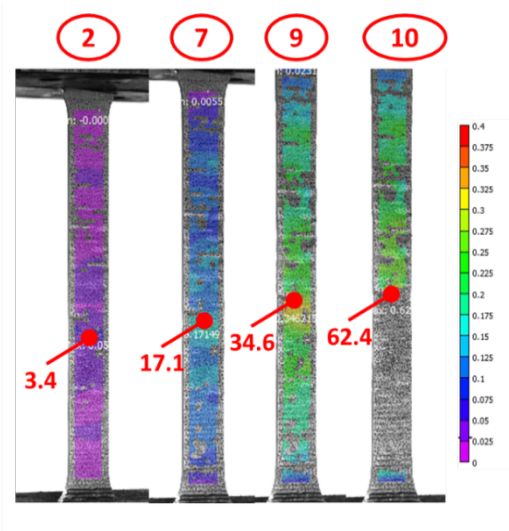

(d)

Figure 17: DIC results for specimens L-longitudinal: (a) machined (M); (b) as-built (R); specimens T-transversal: (c) machined (M); (d) as-built (R).

Specimen ID	**Step**	**ε_m [%]**	**ε_p [%]**	**$(\varepsilon_p - \varepsilon_m)/\varepsilon_p$ [%]**
M-L-A-2	2	0.39	1.02	62
	5	7.42	14.74	50
	8	16.47	34.88	53
	10	20.96	50.88	59
				+56%
R-L-A-8	3	1.32	4.29	69
	8	7.92	15.65	49
	9	11.93	23.44	49
	10	16.70	40.16	58
				+56%
M-T-A-1	2	0.58	1.01	43
	5	7.36	13.12	44
	8	14.59	26.87	46
	10	18.73	43.61	57
				+48%

R-T-A-8	2	1.33	3.41	61
	7	10.49	17.15	39
	9	19.08	34.62	45
	10	21.09	62.63	66
				+53%

Table 8: Comparison of elongations for machined (M) and as-built (R) transversal (T) specimens.

6. Discussion

This section provides a more in-depth interpretation of the results from the geometrical and mechanical characterization (presented in Sections 4 and 5) of WAAM-produced specimens in terms of:

- Assessment of the geometrical irregularities of the cross-section from different measurements;
- Influence of the geometrical irregularities of the cross-section on the key mechanical properties of specimens with different orientations and cooling strategies.

6.1. Geometrical irregularities of the cross-section: comparison between results from different measurements

The detailed characterization of the geometrical irregularities of the cross-section from the surface roughness and thickness of the single specimen from the 3D scanning (Sections 4.1 and 4.2) and the thickness measurements on different samples (Section 4.3) allows to make some interesting considerations on the main features of the printing process in terms of its accuracy and discrepancy between nominal geometry and as-printed one.

6.1.1. Cross-section irregularities for a given specimen

The detailed representation of the upper and lower surfaces through the point-clouds may allow a first estimation of the variability of the thickness from the variability of the two surfaces, represented as random variables (Z_{US} and Z_{LS}). In this way, the standard deviation of the thickness can be estimated from the standard deviation of the two surfaces, whose values were evaluated in terms of root mean square height ($S_{q,US}$ for the upper surface and $S_{q,LS}$ for the lower surface) using the SRSS combination rule, i.e. $\widetilde{\sigma}_t = \sqrt{{S_{q,US}}^2 + {S_{q,LS}}^2}$ (thus assuming that Z_{US} and Z_{LS} are statistically

independent random variables), or a more complex combination accounting for the correlation coefficient ρ_{US} between Z_{US} and Z_{LS}, i.e. $\widehat{\sigma}_t = \sqrt{S_{q,US}{}^2 + S_{q,LS}{}^2 + 2 \cdot \rho_{UL} \cdot S_{q,US} \cdot S_{q,LS}}$. Those estimates can be then compared with the values of $\sigma_{t(x)}$, $\sigma_{t(y)}$ and σ_t obtained from the subset of measures as discribed in Section 4.2.

The values of the standard deviations of the thickness distribution along x and y ($\sigma_{t(x)}$, $\sigma_{t(y)}$) as well as the overall standard deviation σ_t are reported in the histogram of Fig. 18a. The values of the root mean square height ($S_{q,US}$ and $S_{q,LS}$) are reported in the histogram of Fig. 18b together with the SRSS estimate of the thickness standard deviation $\widetilde{\sigma}_t$. As far as the thickness is concerned, the values of standard deviations along the two perpendicular directions $\sigma_{t(x)}$ and $\sigma_{t(y)}$ are of around 0.20 mm leading to a coefficient of variation of around 0.05. Also the value of the overall standard deviation σ_t is of around 0.20 mm thus leading to coefficient of variation of around 0.05.

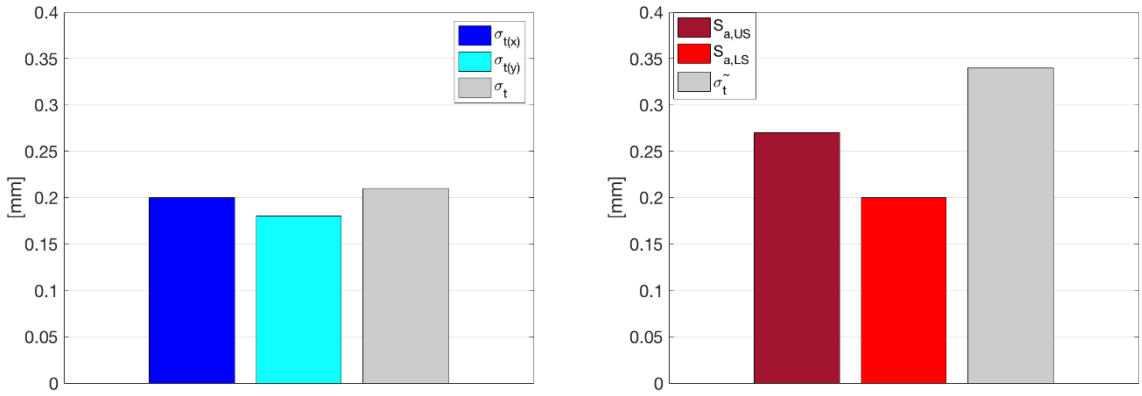

(a) (b)

Figure 18: (a) comparison of standard deviations from thickness values; (b) comparison of root mean square values and estimation of standard deviation from roughness values;

The standard deviation values of the surface roughness (estimated in terms of root mean square height) are around 0.20 mm, while the value of $\widetilde{\sigma}_t$ (SRSS estimate of the thickness standard deviation) is of around 0.35 mm. This value appears quite higher than the value of σ_t (obtained from direct measures of thickness on a sub set of values), thus indicating, as expected, a non-negligible correlation between Z_{US} and Z_{LS}. A first estimation of the correlation coefficient ρ_{UL} may be obtained

by imposing $\widehat{\sigma}_t = \sigma_t$, leading to a positive correlation of around 0.6. This finding further confirms that the main source of variation in thickness is the result of the roughness caused by the deposition of successive layers of material, that creates peaks (i.e. maximum thickness) and pits (i.e. minimum thickness).

6.1.2. Specimen-to-specimen effective thickness variability

The main source of information obtained from the measures of the effective thickness taken on all as-built specimens (as presented in Section 4.3) is summarized in the histograms of Figure 19, reporting the values of the standard deviation $\sigma_{t,eff}$ and the systematic difference $\Delta_{t,eff}$ along L and T (taken as difference between the mean effective thickness $\mu_{t,eff}$ and the nominal thickness t_n).

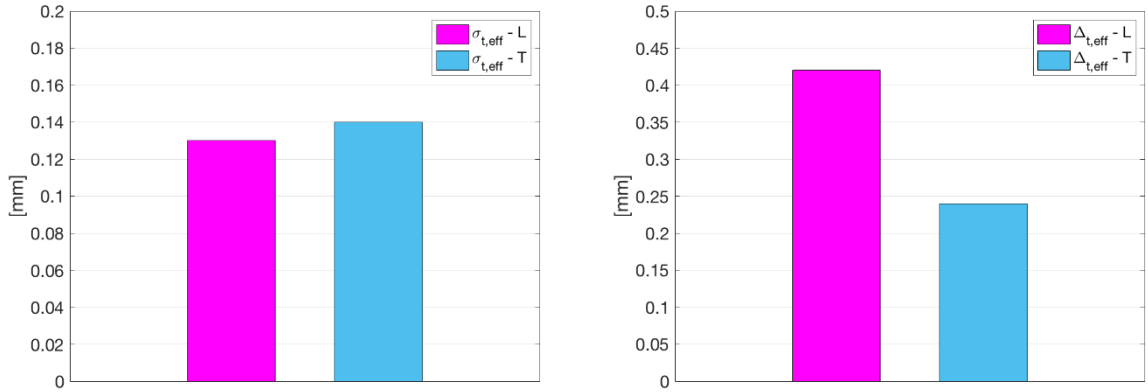

(a) (b)

Figure 19: (a) comparison of standard deviation and (b) systematic difference of effective thickness.

The values of $\sigma_{t,eff}$ along L and T are almost the same (0.13 mm and 0.14 mm, respectively), corresponding to a coefficient of variation of around 0.03-0.04. On the other hand, the values of $\Delta_{t,eff}$ are larger for specimens L (around 0.40 mm) than for specimens T (slightly higher than 0.20 mm). The corresponding relative errors are between 5% (for specimens T) and 10% (for specimens L), with an average of 7.5%. In other terms, the mean value of the ratio between the effective and nominal thickness is equal to 0.90. These results related to the discrepancy between effective and nominal thickness could be properly considered at manufacturing stage. For design purposes, the effective values of thickness and corresponding effective cross-sectional area are suggested to be used.

6.2. Influence of the geometrical irregularities of the cross-section on the mechanical response

The interpretation of the mechanical response from tensile tests focuses specifically on the comparison of the results in terms of surface finishing (machined vs. as-built) and orientation (longitudinal vs. transversal). In particular, the results from specimens realized with active cooling are discussed in Section 6.2.1, while the results from specimens realized with uncontrolled cooling are discussed in Section 6.2.2.

6.2.1. Specimens realized with active cooling process

Figure 20 presents an overview of the mechanical properties of WAAM specimens realized with active cooling, comparing the response of those with machined surface with respect to those with as-built ("rough") surface. Table 9 quantifies the relative differences between the mechanical parameters comparing both machined vs as-built ("rough") specimens (for the same orientation) and transversal vs longitudinal orientations.

Overall, the variations of the mechanical properties from as-built and machined specimens oriented longitudinally (L) are negligible. Specimens oriented transversally (T) present instead 5% increase in Young's modulus when tested as-built with respect to the machined values, as well as 8% reduction in yielding (0.2% proof stress). For both directions, the elongation at rupture decreases for the as-built specimens (-8% for L specimens and -17% for T specimens). It should be noted that these variations lie within the standard deviations of the distribution of the test results, thus suggesting that the influence of the geometrical irregularities in the as-built specimens is rather small.

Kyvelou et al. [7] reported similar comparisons between as-built and machined specimens realized with WAAM stainless steel. The trends for 0.2% proof stress and elongation at rupture are similar to the ones obtained in the present work. However, the registered decrease in Young's modulus of as-built material relative to the machined one as reported in [7] cannot be appreciated in the results reported here. The higher discrepancies of the machined vs. as-built mechanical properties reported in [7] might be related to the thickness of the printed plates. Thus, further explorations on this specific aspect should be developed in detail.

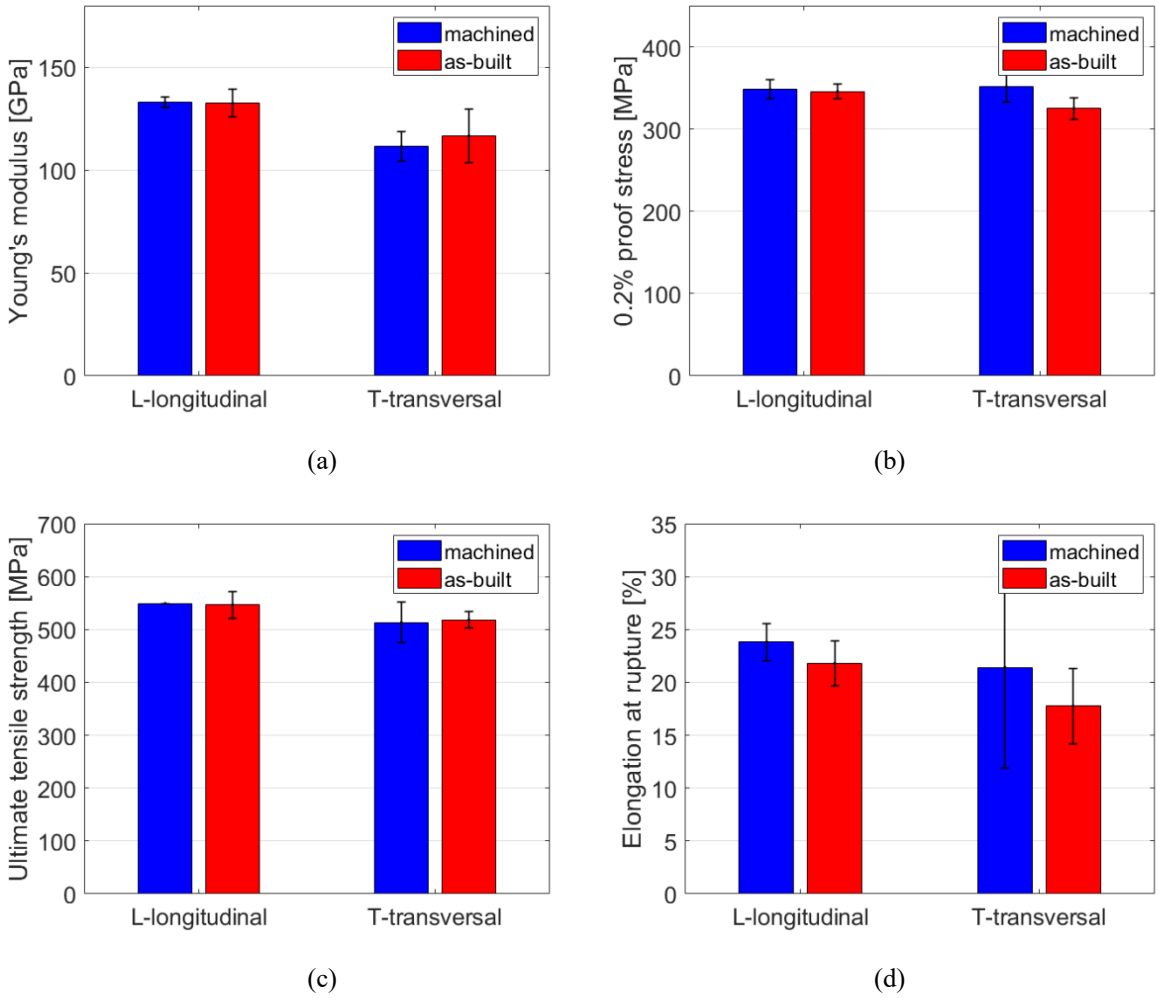

Figure 20: Comparison of WAAM mechanical properties for machined and as-built specimens with active cooling: (a) Young's modulus, (b) 0.2% proof stress, (c) ultimate tensile strength, (d) elongation at rupture.

		E [GPa]	**$R_{p0.2}$ [MPa]**	**UTS [MPa]**	**$A_{\%}$ [%]**	**$R_{p0.2}$/ UTS [-]**
(R-M)/M	L	0%	-1%	0%	-8%	0%
	T	+5%	-8%	+1%	-17%	-9%
(L-T)/T	M	+19%	-1%	+7%	+11%	-8%
	R	+14%	+6%	+5%	+23%	+1%

Table 9: Comparison of mechanical properties for specimens with active cooling.

Comparing the mechanical properties for the two directions, it appears that:

- In general, the longitudinal specimens (L) have higher values of all mechanical properties than the transversal ones (T), both in case of machined and as-built specimens.
- The main differences are observed for the Young's modulus values (+19% for machined specimens and +14% for as-built ones) and for the elongation at rupture (+11% for machined specimens and +23% for as-built ones).

These results further confirm the evidence also presented in Section 3.1 regarding the intrinsic anisotropy of WAAM stainless steel, resulted from the microstructural characterization, with no distinct reference to the geometrical irregularities of the printed outcomes. This is also evidenced in [6,14,16,17].

6.2.2. Specimens realized with uncontrolled cooling process

Figure 21 presents the mechanical properties of both orientations comparing the results for machined and as-built specimens. In Table 10 the relative differences are proposed both between machined and as-built specimens, for the same orientation, and between the two different orientations.

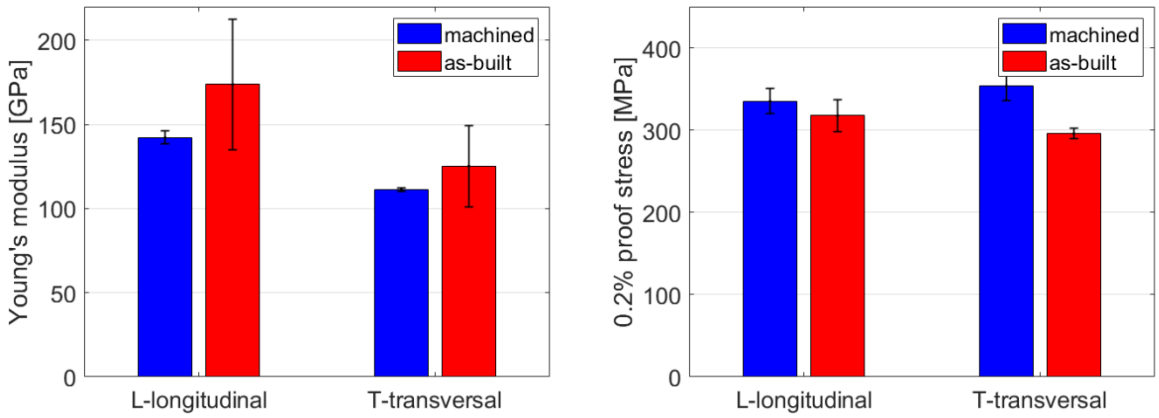

(a) (b)

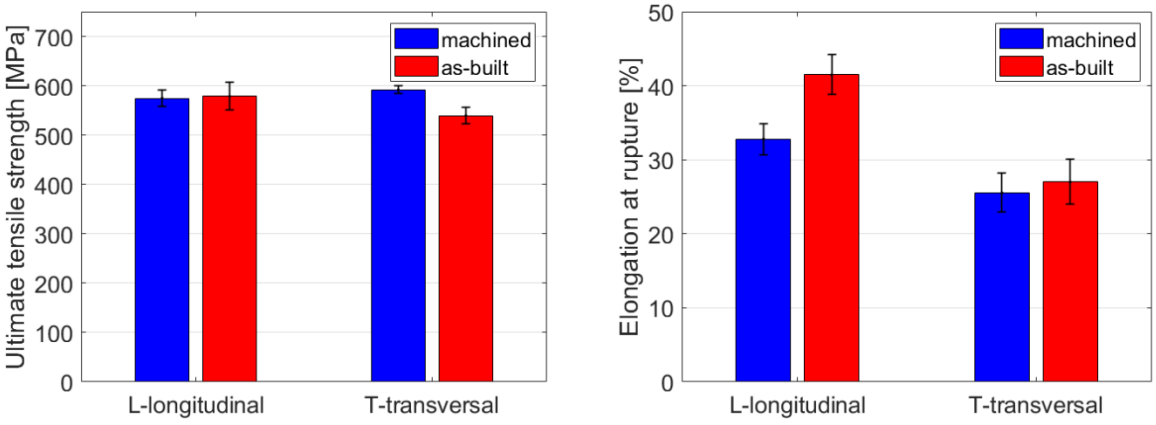

(c) (d)

Figure 21: Comparison of WAAM mechanical properties for machined and as-built specimens with uncontrolled cooling: (a) Young's modulus, (b) 0.2% proof stress, (c) ultimate tensile strength, (d) elongation at rupture.

		E [GPa]	**$R_{p0.2}$ [MPa]**	**UTS [MPa]**	**$A_{\%}$ [%]**	**$R_{p0.2}$/ UTS [-]**
(R-M)/M	L	+22%	-5%	+1%	+26%	-6%
	T	+13%	-16%	-9%	+6%	-8%
(L-T)/T	M	+28%	-5%	-3%	+28%	-2%
	R	+39%	+7%	+7%	+54%	0%

Table 10: Comparison of mechanical properties for specimens with uncontrolled cooling.

Differently from the specimens printed with active cooling (Section 6.2.1), the variations computed for the specimens with uncontrolled cooling are higher and with no clear pattern. This might be due to the higher variability of the mechanical properties of the base material within each type of specimen (as also described in Section 5.1), which also affects the comparison. Thus, further studies would be required to deeply analyze the influence of cooling strategy in the material characteristics from both the microstructural and mechanical point of view.

7. Conclusions

The study presents the results of the research work aimed at (i) characterizing the geometrical irregularities proper of Wire-and-Arc Additively Manufactured (WAAM) stainless steel structural members and (ii) evaluating their possible influence on the mechanical properties. Indeed, given the rough geometry of the printed outcomes, the non-uniform distribution of cross-sectional area may result in a non-uniform stress field and related effects on the mechanical properties of structural elements. As such, proper characterization of the geometrical discrepancy is the fundamental step to study the structural behavior of WAAM-produced elements. The study considered planar elements manufactured with the continuous printing strategy and allows to draw the conclusions listed below.

Geometrical characterization of planar elements:

- The manufacturing process is characterized by a limited precision resulting in a non-negligible surface roughness.
- For a given specimen, the surface roughness of the top and bottom faces, treated as two individual random processes, are characterized by root mean square heights in the order of 0.20-0.30 mm and maximum peak and pit values of around 0.8 mm.
- This surface roughness leads to a thickness variability of the given specimen (of average thickness of around 4 mm) having a coefficient of variation of around 0.05.
- This thickness variability shows different features along the printing direction (longitudinal) and perpendicular to it (transversal), even though the order of magnitude remains the same. The assessment of the thickness variability leads to an indirect evaluation of the coefficient of correlation between upper and lower surface roughness which turns out to be around 0.6.
- The specimen-to-specimen effective (average) thickness shows a coefficient of variation of around 0.03-0.04.
- The mean value of the ratio between the effective and nominal thickness is equal to 0.90.

Influence of the geometrical irregularities on the mechanical properties of planar elements (for active cooling only):

- Along the longitudinal direction, the geometrical irregularities do not seem to significantly affect the mechanical properties of the specimens, as machined and as-built specimens provided similar results.
- Along the transversal direction, the geometrical irregularities do seem to negatively impact the mechanical properties of the specimens. More in detail:

- The yield strength of the "rough" specimen is almost 10% lower than the one of the equivalent (same effective cross section) machined specimen as obtained multiplying the effective cross section by the material 0.2% proof stress.
- The elongation at rupture of the "rough" specimen is almost 20% lower than the one of the equivalent (same effective cross section and length) machined specimen.

The specimens printed with uncontrolled cooling showed higher variations in the mechanical parameters, with no clear pattern. This might also be due to the higher variability of the mechanical properties of the base material within each type of specimen, which also affects the comparison. This last aspect suggests the need of specific investigations on the influence of printing cooling strategy in the material characterization of WAAM-produced stainless steel.

It should be finally noted that the above concluding remarks refer to the printed outcomes realized with a specific set of parameters (as listed in Section 2.1). Clearly, in order to generalize these results, additional investigations are required to study the influence of the process parameters in the mechanical and geometrical characterization of WAAM-produced stainless steel.

Acknowledgements

The support of Dutch company MX3D held in Amsterdam is gratefully acknowledged for giving the additive-manufactured elements tested.

The authors would like to acknowledge the work done by Lavinia Tonelli and Lorella Ceschini from the Metallurgic department of University of Bologna for the microstructural analyses.

References

[1] S.W. Williams, F. Martina, A.C. Addison, J. Ding, G. Pardal, P. Colegrove, Wire + Arc additive manufacturing, Mater. Sci. Technol. (United Kingdom). 32 (2016) 641–647. https://doi.org/10.1179/1743284715Y.0000000073.

[2] T.A. Rodrigues, V. Duarte, R.M. Miranda, T.G. Santos, J.P. Oliveira, Current status and perspectives on wire and arc additive manufacturing (WAAM), Materials (Basel). 12 (2019). https://doi.org/10.3390/ma12071121.

[3] M. Dinovitzer, X. Chen, J. Laliberte, X. Huang, H. Frei, Effect of wire and arc additive manufacturing (WAAM) process parameters on bead geometry and microstructure, Addit. Manuf. 26 (2019) 138–146. https://doi.org/10.1016/j.addma.2018.12.013.

[4] C. Buchanan, L. Gardner, Metal 3D printing in construction: A review of methods, research, applications, opportunities and challenges, Eng. Struct. 180 (2019) 332–348. https://doi.org/10.1016/j.engstruct.2018.11.045.

[5] C. Buchanan, V.P. Matilainen, A. Salminen, L. Gardner, Structural performance of additive manufactured metallic material and cross-sections, J. Constr. Steel Res. 136 (2017) 35–48. https://doi.org/10.1016/j.jcsr.2017.05.002.

[6] L. Gardner, P. Kyvelou, C. Buchanan, Testing of wire and arc additively manufactured tubular sections, (2019)

978–981. https://doi.org/10.3850/978-981-11-0745-0.

[7] P. Kyvelou, H. Slack, D.D. Mountanou, M.A. Wadee, T. Ben Britton, C. Buchanan, L. Gardner, Mechanical and microstructural testing of wire and arc additively manufactured sheet material, Mater. Des. (2020) 108675. https://doi.org/10.1016/J.MATDES.2020.108675.

[8] X. Xu, G. Mi, Y. Luo, P. Jiang, X. Shao, C. Wang, Morphologies, microstructures, and mechanical properties of samples produced using laser metal deposition with 316 L stainless steel wire, Opt. Lasers Eng. 94 (2017) 1–11. https://doi.org/10.1016/j.optlaseng.2017.02.008.

[9] X. Xu, S. Ganguly, J. Ding, S. Guo, S. Williams, F. Martina, Microstructural evolution and mechanical properties of maraging steel produced by wire + arc additive manufacture process, Mater. Charact. 143 (2018) 152–162. https://doi.org/10.1016/j.matchar.2017.12.002.

[10] J. Ge, J. Lin, Y. Chen, Y. Lei, H. Fu, Characterization of wire arc additive manufacturing 2Cr13 part: Process stability, microstructural evolution, and tensile properties, J. Alloys Compd. 748 (2018) 911–921. https://doi.org/10.1016/j.jallcom.2018.03.222.

[11] J. V. Gordon, C. V. Haden, H.F. Nied, R.P. Vinci, D.G. Harlow, Fatigue crack growth anisotropy, texture and residual stress in austenitic steel made by wire and arc additive manufacturing, Mater. Sci. Eng. A. 724 (2018) 431–438. https://doi.org/10.1016/j.msea.2018.03.075.

[12] W. Wu, J. Xue, L. Wang, Z. Zhang, Y. Hu, C. Dong, Forming process, microstructure, and mechanical properties of thin-walled 316L stainless steel using speed-cold-welding additive manufacturing, Metals (Basel). 9 (2019). https://doi.org/10.3390/met9010109.

[13] N. Rodriguez, L. Vázquez, I. Huarte, E. Arruti, I. Tabernero, P. Alvarez, Wire and arc additive manufacturing: a comparison between CMT and TopTIG processes applied to stainless steel, Weld. World. 62 (2018) 1083–1096. https://doi.org/10.1007/s40194-018-0606-6.

[14] L. Ji, J. Lu, C. Liu, C. Jing, H. Fan, S. Ma, Microstructure and mechanical properties of 304L steel fabricated by arc additive manufacturing, MATEC Web Conf. 128 (2017). https://doi.org/10.1051/matecconf/201712803006.

[15] C. V. Haden, G. Zeng, F.M. Carter, C. Ruhl, B.A. Krick, D.G. Harlow, Wire and arc additive manufactured steel: Tensile and wear properties, Addit. Manuf. 16 (2017) 115–123. https://doi.org/10.1016/j.addma.2017.05.010.

[16] V. Laghi, M. Palermo, L. Tonelli, G. Gasparini, L. Ceschini, T. Trombetti, Tensile properties and microstructural features of 304L austenitic stainless steel produced by wire-and-arc additive manufacturing, Int. J. Adv. Manuf. Technol. (2020) 3693–3705. https://doi.org/10.1007/s00170-019-04868-8.

[17] V. Laghi, M. Palermo, G. Gasparini, V.A. Girelli, T. Trombetti, Experimental results for structural design of Wire-and-Arc Additive Manufactured stainless steel members, J. Constr. Steel Res. 167 (2020) 105858. https://doi.org/10.1016/j.jcsr.2019.105858.

[18] V. Laghi, M. Palermo, G. Gasparini, V.A. Girelli, T. Trombetti, Geometrical characterization of Wire-and-Arc Additive Manufactured steel elements, VBRI Press Adv. Mater. Lett. 10 (2019) 695–699.

[19] MX3D Webpage, (n.d.). www.mx3d.com.

[20] Oerlikon, (n.d.). https://www.oerlikon.com/en/.

[21] L. Gardner, P. Kyvelou, G. Herbert, C. Buchanan, Testing and initial verification of the world's first metal 3D printed bridge, J. Constr. Steel Res. 172 (2020). https://doi.org/10.1016/j.jcsr.2020.106233.

[22] ISO, BSI Standards Publication Geometrical product specifications (GPS) — Surface texture : Areal Part 2 : Terms , definitions and surface, (2012).

[23] Artec 3D webpage, (n.d.). https://www.artec3d.com.

[24] Metallic materials — Tensile testing — Part 1: Method of test at room temperature Matériaux métalliques — Essai de traction — Partie 1: Méthode d'essai à température ambiante (2009). http://files.instrument.com.cn/FilesCenter/20090913/200991371610112081.pdf.

[25] DIN EN 10002-1:2001, Metallic materials - Tensile testing, Met. Mater. - Tensile Test. (2001) 54.

[26] W. Ramberg, W.R. Osgood, Description of stress-strain curves by three parameters, (1943).

[27] K.J.R. Rasmussen, Full-range stress-strain curves for stainless steel alloys, Res. Rep. - Univ. Sydney, Dep. Civ. Eng. 59 (2001) 1–44.

[28] L. Gardner, M. Ashraf, Structural design for non-linear metallic materials, Eng. Struct. 28 (2006) 926–934. https://doi.org/10.1016/j.engstruct.2005.11.001.

[29] European Committee for Standardization (CEN), EN 1993 1-4: Eurocode 3 - Design of steel structures, part 1-4: General rules, supplementary rules for stainless steel, (2015).

Appendix A

(Y) Realization number	1	2	3	4	5	6	7	8	9	10	11	12	13	14
1	1.00	0.37	-0.56	-0.29	0.26	0.28	0.45	0.44	0.08	0.10	-0.45	0.22	0.38	-0.08
2		1.00	-0.22	0.10	0.25	-0.13	0.24	-0.11	0.35	0.12	-0.10	-0.09	0.33	0.21
3			1.00	0.08	-0.39	0.06	-0.25	-0.49	-0.15	0.11	0.12	0.31	0.05	0.30
4				1.00	0.29	0.32	-0.25	-0.07	0.08	-0.16	0.04	-0.06	-0.28	-0.08
5					1.00	0.04	0.55	0.11	0.29	0.22	-0.20	-0.13	-0.19	-0.21
6						1.00	-0.07	0.15	0.01	-0.17	-0.25	0.36	0.10	-0.07
7							1.00	-0.02	0.09	0.09	-0.47	0.05	0.19	0.20
8								1.00	0.13	-0.46	-0.34	0.10	0.25	-0.05
9									1.00	-0.22	-0.20	0.03	-0.09	0.13
10										1.00	0.53	-0.15	-0.26	-0.18
11											1.00	-0.37	-0.30	-0.07
12												1.00	0.42	-0.19
13													1.00	0.29
14														1.00

Table A1: Correlation coefficients matrix between all realizations (symmetrical). Yellow to red colors are for positive values, light blue to blue colors are for negative values.

(X) Section number	1	2	3	4	5	6	7	8	9	10	11	12
1	1,00	0,27	0,01	0,40	0,66	0,45	0,31	0,47	0,48	0,44	0,02	0,06
2		1,00	0,68	-0,29	0,53	0,70	0,50	0,56	0,70	0,27	0,48	0,23
3			1,00	-0,10	0,30	0,68	0,57	0,20	0,60	-0,18	0,53	0,09
4				1,00	0,47	0,12	-0,01	0,10	0,17	0,26	0,16	-0,01
5					1,00	0,68	0,30	0,54	0,78	0,44	0,28	0,21
6						1,00	0,72	0,63	0,86	0,39	0,35	0,30
7							1,00	0,58	0,65	0,27	0,09	0,35
8								1,00	0,72	0,44	0,29	0,71
9									1,00	0,35	0,21	0,48
10										1,00	0,04	0,20
11											1,00	0,28
12												1,00
13												
14												
15												
16												
17												

18
19
20
21
22
23

1

Section number	**13**	**14**	**15**	**16**	**17**	**18**	**19**	**20**	**21**	**22**	**23**
1	-0,06	0,07	-0,09	0,18	0,00	0,21	0,29	0,17	-0,44	-0,36	0,09
2	0,39	0,44	0,56	0,39	0,20	0,41	0,36	0,66	0,58	-0,28	0,22
3	0,58	0,41	0,46	-0,01	0,19	0,01	0,09	0,48	0,40	-0,19	0,31
4	-0,07	-0,05	-0,08	-0,16	-0,40	-0,07	0,09	-0,09	-0,55	-0,33	0,02
5	0,22	0,24	0,37	0,39	-0,15	0,30	0,52	0,46	0,03	-0,51	-0,03
6	0,55	0,57	0,33	0,49	0,17	0,35	0,50	0,71	0,24	-0,12	0,30
7	0,46	0,58	0,15	0,45	0,39	0,36	0,50	0,36	0,02	0,02	0,44
8	-0,02	0,33	0,24	0,43	0,26	0,48	0,47	0,46	0,19	-0,23	0,49
9	0,45	0,56	0,53	0,53	0,26	0,45	0,60	0,63	0,35	-0,38	0,35
10	0,27	0,59	0,31	0,71	-0,01	0,74	0,72	0,21	0,01	0,15	0,25
11	0,11	0,09	0,33	-0,23	-0,04	0,04	-0,12	0,22	0,23	-0,11	0,31
12	-0,06	0,25	0,26	0,35	0,50	0,36	0,42	0,25	0,37	0,16	0,48
13	1,00	0,83	0,51	0,50	0,43	0,55	0,27	0,18	0,35	0,03	0,23
14		1,00	0,67	0,65	0,47	0,82	0,55	0,15	0,37	0,07	0,61
15			1,00	0,32	0,14	0,56	0,44	0,14	0,63	-0,27	0,49
16				1,00	0,37	0,77	0,78	0,42	0,37	0,21	0,04
17					1,00	0,52	0,03	-0,04	0,33	0,15	0,38
18						1,00	0,52	0,05	0,32	-0,05	0,46
19							1,00	0,42	0,25	0,21	0,18
20								1,00	0,51	0,04	-0,12
21									1,00	0,11	0,13
22										1,00	-0,03
23											1,00

2 *Table A2: Correlation coefficients matrix between all sections across the ensemble (symmetrical). Yellow to*
3 *red colors are for positive values, light blue to blue colors are for negative values.*

4